MULTISCALE MODEL. SIMUL.
Vol. 22, No. 1, pp. 436–475

UPSCALING AN EXTENDED HETEROGENEOUS STEFAN PROBLEM FROM THE PORE-SCALE TO THE DARCY SCALE IN PERMAFROST*

MALGORZATA PESZYNSKA†, NAREN VOHRA†, AND LISA BIGLER‡

Abstract. In this paper we upscale thermal models from the pore–scale to the Darcy scale for applications in permafrost. We incorporate thawing and freezing of water at the pore-scale and adapt rigorous homogenization theory from [A. Visintin, *SIAM J. Math. Anal.*, 39 (2007), pp. 987–1017] to the original nonlinear multivalued relationship to derive the effective properties. To obtain agreement of the effective model with the known Darcy scale empirical models, we revisit and extend the pore-scale model to include the delicate microscale physics in small pores. We also propose a practical reduced model for the nonlinear effective conductivity. We illustrate with simulations.

Key words. heterogeneous Stefan problem, homogenization, upscaling, permafrost models, porous media, pore-scale and Darcy scale, nonlinear degenerate parabolic partial differential equation

MSC codes. 35B27, 35R35, 80A22, 76S05

DOI. 10.1137/23M1552000

1. Introduction.

In this paper we apply numerical upscaling to connect the permafrost models at the macro- (Darcy) scale to the micro- (pore-scale) processes. Permafrost is the ground that remains frozen for two or more years, and is a complex environment with great importance to climate studies. Our focus in this paper is on the energy equation and on the freezing/thawing phenomena; other equations as well as the coupled thermal-hydrological processes will be discussed elsewhere.

The following energy equation combines the conservation of energy with Fourier law:

$$\partial_t w + \nabla \cdot q = f, \quad q = -k(\theta)\nabla\theta, \quad w = \alpha(\theta), \tag{1.1}$$

and requires constitutive equations defining the enthalpy w and heat conductivity k as functions of temperature θ. The models of phase change are challenging since $w(\theta)$ is typically multivalued at the temperature of phase change; this feature has been very well studied, in particular, for the well-known Stefan problem in which $w \in \alpha(\theta) = c(\theta)\theta + L\mathcal{H}(\theta)$ where $\mathcal{H}$ is the Heaviside graph, and c, L are the positive heat capacity and nonnegative latent heat coefficients [73, 65]. In what follows we write $w \in \alpha(\theta)$ when $\alpha(\theta)$ is multivalued, and $w = \alpha(\theta)$ if the relationship in some particular material is single-valued.

Permafrost soil is a porous medium, a mixture of $N_{MAT} = 2$ materials: rock and water in liquid and ice phases: in this paper we do not consider vapor phase or air

*Received by the editors February 8, 2023; accepted for publication (in revised form) August 23, 2023; published electronically March 6, 2024.
https://doi.org/10.1137/23M1552000
Funding: This research was partially supported by the grants NSF DMS-1912938 "Modeling with Constraints and Phase Transitions in Porous Media", and NSF DMS-1522734 "Phase Transitions in Porous Media across Multiple Scales", PI: Malgorzata Peszynska.
†Department of Mathematics, Oregon State University, Corvallis, OR 97331-4605 USA (mpesz@math.oregonstate.edu, vohran@oregonstate.edu).
‡Department of Mathematics, Oregon State University, Corvallis, OR 97331-4605 USA, and Sandia National Laboratories, Albuquerque, NM 87197-6066 USA (biglerli@oregonstate.edu).

component, and neglect the density variations between ice and water. The energy equation for this mixture depends on the material and on the scale. We consider the pore-scale domains ω and the Darcy-scale domains Ω and work with models denoted by Model-ω and Model-Ω at the pore-scale and the Darcy scale, respectively, in several variants. Each Model-ω recognizes the interface between the materials and phases, and for each material $m = 1, \dots N_{MAT}$ they feature material-specific multivalued relationships $\alpha^{(m)}(\theta)$ as well as conductivities $k^{(m)}(\theta)$. At the Darcy scale, the applications literature commonly uses various experimentally calibrated models which we call Model-Ω-empirical with single-valued functions $\alpha^P(\theta)$ and $k^P(\theta)$; here, the superscript ^{P} refers to the Permafrost, and can be replaced by superscript ^{model} for a particular parametric model.

We devote this paper to the development of the rigorous connection between Model-ω involving the collections $(\alpha^{(m)}, k^{(m)})_m$, and the Darcy-scale Model-Ω-empirical involving (α^P, k^P). We follow the general homogenization theory in [73] to derive Model-Ω with multivalued $\alpha_{eff}(\theta)$ and $k_{eff}(\theta)$ from Model-ω. However, upscaling Model-ω which involves only rock and bulk water (and which we call Model-ω-basic) does not give relationships qualitatively consistent with Model-Ω-empirical. To improve, we propose a new Model-ω-extended which incorporates realistic physics of Gibbs–Thomson relationship to account for the depression of freezing temperature in small pores. After upscaling Model-ω-extended, we get Model-Ω-extended with qualitative agreement with the empirical Model-Ω-empirical. The roadmap we follow is summarized in Table 1.

We illustrate the findings with computations and provide ample references to both mathematical and applications literature including the emerging work on imaging permafrost soils.

The outline of this paper is as follows. We provide preliminary notation in section 2.1, and give details on Model-ω and Model-Ω-empirical in section 2. In section 3 we explain the process of upscaling of the constitutive relationships from the pore-scale Model-ω-basic and Model-ω-extended to the Darcy-scale Model-Ω-basic and Model-Ω-extended, respectively; we also address approximate Model-Ω-extended-fit, and compare to Model-Ω-empirical. We divide the presentation there into that for α and k. In section 5 we outline the computational models and present simulation results including a comparison of the pore- and the Darcy-scale solutions in section 5.4. We also provide supplementary material (Supplement.pdf [local/web 19.4MB]) with illustrations of the heterogeneous Stefan problem; these provide additional illustrations on the heterogeneous Stefan problem which are not available in the literature.

TABLE 1

Scales: the pore-scale ω and the Darcy scale Ω, and models Model-ω and Model-Ω, respectively, considered in this article. In the last column we indicate the relationship $\alpha(\cdot)$ and whether it is multivalued or single valued for a given collection of models.

Model	Scale	N_{MAT}	Materials	k	α
Model-ω-basic	pore-scale	2	rock (r), water (w)	$k^{(m)}$	$\alpha^{(m)}$, multi
Model-ω-extended	pore-scale	$N_{WMAT} + 1 > 2$	rock (r), and water in pore subdomains $1 \dots N_{WMAT}$		
Model-Ω-basic	Darcy	averaged over (r,w)		k_{eff}	α_{eff}, multi
Model-Ω-extended	Darcy	averaged over (r,$w^{(1)}, \dots w^{(N_{WMAT})}$)			
Model-Ω-extended-fit	Darcy	approximation/fit of Ω-extended		$\widetilde{k_{eff}}$	$\widetilde{\alpha_{eff}}$, single
Model-Ω-empirical	Darcy	calibrated experimentally		k^P	α^P, single

2. Physical models for heat conduction at the Darcy and the pore-scale. We start with general notation in section 2.1 and next we define the heat conduction models at the pore-scale in section 2.2 and at the Darcy scale in section 2.3. A list of parameters and variables is given in Table 2.

2.1. Notation in heat conduction models with phase change. We consider heat conduction in a domain $\Omega \subset \mathbb{R}^d, d \geq 1$, and denote by $\Omega_T = \Omega \times (0,T)$ the space-time cylinder. The boundary of Ω is denoted by $\partial\Omega$, and n is the unit outward normal to $\partial\Omega$; $\partial\Omega$ is partitioned to the Dirichlet boundary $\partial\Omega_D$ and Neumann boundary $\partial\Omega \setminus \partial\Omega_D$. We will also assume that $|\partial\Omega_D| > 0$. We adopt the usual notation on Sobolev spaces [66, 72], and denote for shorthand the Sobolev spaces on Ω_T as follows: $v \in L^2(H^1)$ denotes functions $v \in L^2(0,T;H^1(\Omega))$. For a set S, $D(S) = C_0^\infty(S)$ is the set of smooth functions with compact support on S, and $D(S)'$ is the space of distributions, i.e., the continuous linear functionals on $D(S)$. Further, we denote by $|S|$ the measure of set S and by $\bar{S}$ its closure.

We also recall the Heaviside function $H : \mathbb{R} \to \{0,1\}$, $H(0,\infty) = \{1\}; H(-\infty,0] = \{0\}$, and define the multivalued Heaviside graph as follows: $\mathcal{H}(0,\infty) = \{1\}; \mathcal{H}(-\infty,0) = \{0\}; \mathcal{H}(0) = [0,1]$.

2.1.1. Heat conduction with phase change in a single material. We now provide details of (1.1) which involves the energy density (enthalpy) w, the heat flux q, the temperature θ, and the liquid phase fraction $\chi(\theta)$. The data are the source term f and heat conductivity k. We assume that Ω has a fixed volume; in particular, we disregard the change of volume due to ice expansion as the water freezes. We also ignore convection. We consider two phases: liquid and ice (solid), and their properties are denoted with subscript $_l$ for liquid, and $_i$ for ice. The domain Ω is partitioned into the liquid Ω_l and ice phase subdomains Ω_i separated by an interface ("mushy") region Ω_{li} in which ice and liquid co-exist.

First, we require a definition of w. Without the phase change $dw = c(\theta)d\theta$, with heat capacity c, and $w = \alpha(\theta) = \mathcal{C}(\theta) = \int_{\theta_{ref}}^{\theta} c(v)dv$ where θ_{ref} can be any convenient reference temperature which we choose to be equal 0; for freezing/thawing, the

TABLE 2
Variables and parameters used throughout this article.

Notation	Description	
$p \in \{i,\ l\}$	Subscript: phase p either solid ice i (frozen), or liquid l (unfrozen)	
(m)	Superscript: material m; for example, water (w), rock grains (r)	
$\eta,\ \eta^{(m)}$	Volume fraction of material (m)	
$\omega,\ \omega_p^{(m)}$	An REV ω and $\omega_p^{(m)} \subset \omega$ is the portion of the REV occupied by phase p of material(m)	
Variable	Description/SI Unit	
w	Enthalpy/Energy per unit volume [J/m^3]	
θ	Temperature [°C]	
χ_l	Liquid phase fraction $(= \chi_l^{(w)})$ [−]	
Parameter	Description/SI Unit	Typical value
η	Porosity [−]	Sand $[0.30, 0.35]$, Silt $[0.4, 0.5]$, Clay $[0.45, 0.55]$ [4](Pg. 74)
θ_*	Freezing point depression [°C]	$[0, -5]$ [1](Pg. 24)
c	Volumetric heat capacity [J/m^3°C]	Water 4.19×10^6, Ice 1.90×10^6 [58]
k	Thermal conductivity [J/m s°C]	Water 0.58, Ice 2.3 [58]
L	Latent heat per unit volume [J/m^3]	Water 3.06×10^8 [58]

reference temperature is best set to the freezing temperature θ_*. For heat capacities constant in each phase, we set $\mathcal{C}(\theta) = (\theta - \theta_*)\begin{cases} c_l, \theta > \theta_* \\ c_i, \theta < \theta_* \end{cases}$. We assume local equilibrium, i.e., that $\theta|_{\Omega_l} > \theta_*$, $\theta|_{\Omega_i} < \theta_*$, and that $\theta|_{\Omega_{li}} = \theta_*$. We need both χ and θ as independent variables to fully describe the system's state, but $\chi|_{\Omega_l} = 1$, $\chi|_{\Omega_i} = 0$, while $\chi \in [0,1]$ in Ω_{li}. We write concisely $\chi(\theta) \in \mathcal{H}(\theta - \theta_*)$.

The well-known Stefan problem [72, 18] describes the phase change between ice i and liquid l: the melting requires adding some latent heat L amount, and the freezing is exothermic. This is encapsulated in the definition of enthalpy

$$w \in \alpha(\theta) = \int_{\theta_*}^{\theta} c(v)dv + L\chi(\theta) = \mathcal{C}(\theta) + L\mathcal{H}(\theta - \theta_*). \tag{2.1}$$

Formally, α is the subdifferential of the convex function, the primitive ψ of $\alpha = \partial\psi$ given by

$$\psi(\theta) = \begin{cases} \frac{c_i}{2}(\theta - \theta_*)^2, & \theta < \theta_*, \\ \frac{c_l}{2}(\theta - \theta_*)^2 + L(\theta - \theta_*), & \theta \geq \theta_*. \end{cases} \tag{2.2}$$

To complete the model we have as in [72] $k(\theta) = \begin{cases} k_i, & \theta < \theta_* \\ k_l, & \theta > \theta_* \end{cases}$, $k(\theta_*) = \frac{k_l + k_i}{2}$. We also require some initial and boundary conditions. Let w_{init} be given, and we set $w(x,0) = w_{init}(x)$. We also set Dirichlet boundary conditions for $\theta|_{\partial\Omega_D}$, and Neumann conditions for $q \cdot n|_{\partial\Omega \setminus \partial\Omega_D}$.

In summary, the model, in the sense of distributions, is

$$\partial_t(w(x,t)) - \nabla \cdot (k(\theta)\nabla\theta) = f, \quad w \in \alpha(\theta) = \partial\psi(\theta) \text{ in } D(\Omega_T)'. \tag{2.3}$$

One well known interpretation of (2.3) is that if the mushy region is reduced to an interface $\Omega_{li} = \Gamma_{li} = \partial\Omega_l \cap \partial\Omega_i$, the Stefan problem describes the heat conduction in each Ω_l and Ω_i coupled by the Stefan condition $[q \cdot n]|_{\Gamma_{li}} = Lv$, where v is the speed of the free boundary $\Gamma_{li} = \Gamma_{li}(t)$, and where $\mathcal{H}(\cdot)$ is replaced by $H(\cdot)$ [65]. For numerical simulations which approximate θ, w, χ, it is natural and necessary to accept that $\chi \in [0,1]$ rather than only $\chi \in \{0,1\}$: except in front-tracking approaches such as [37, 17], the position of free boundary is usually not aligned with the degrees of freedom.

The analysis of (2.3) is well established; we refer to [72, 18] for extensive analysis and references, and to [66, 65] for the connection between the classical problem, Stefan condition, mushy region, and the weak formulation. The regularity of solutions is typically low due to the free boundary where the fluxes take a jump. For example, under homogeneous Dirichlet boundary conditions with sufficiently smooth initial data one finds [73, 72] that $\theta \in L^2(H_0^1)$ while $w \in L^2(\Omega_T)$.

2.1.2. Multiple materials and thermal properties. Now we assume that the domain Ω is filled by N_{MAT} distinct materials $m = 1, \dots N_{MAT}$ such as rock or water, each associated with a subdomain $\Omega^{(m)}$. We also denote the space-time cylinders $\Omega_T^{(m)} = \Omega^{(m)} \times (0,T)$. The material interfaces are fixed; for an interface between some $\Omega^{(m)}, \Omega^{(j)}$ we denote the interface by $\Gamma^{(mj)} = \partial\Omega^{(m)} \cap \partial\Omega^{(j)}$. These materials are in the liquid $p = l$ phase, or in the ice $p = i$ phase; we denote their thermal properties with superscript $^{(m)}$ and subscript $_p$.

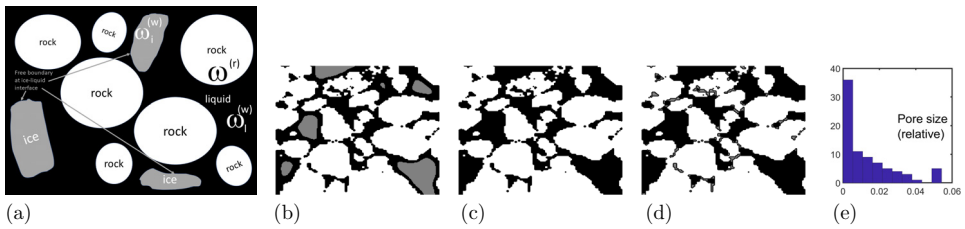

(a) (b) (c) (d) (e)

FIG. 1. *Illustration of the pore-scale domain* ω *with rock* $\omega^{(r)}$ *in white, liquid* $\omega_l^{(w)}$ *in black. In* (a)–(c) *gray denotes* $\omega_i^{(w)}$. *In* (d) (a) *Cartoon with notation.* (b)–(d)*: image of sandstone geometry from* [50] (b) *with ice,* (c) *without ice, and* (d) *without ice, but small pores marked by gray found with a heuristic algorithm* (e) *the histogram of pore distribution in* (c).

In this paper we are interested in the particular composite material: a soil mixture of rock grains ($m = r$) and water-filled pore space ($m = w$) in phase $p = l$ or $p = i$; see Figure 1. The geometry of Ω is known from X-ray micro-CT [49, 14, 59], and there is abundant work on modeling and upscaling flow (but not energy) models from the pore- to the Darcy scale; see, e.g., [69, 10], and our own work in [12, 50, 64] on this subject. In this paper we will consider two classes of models at the pore-scale, Model-ω-basic, and Model-ω-extended, in which we will consider a mixture of rock and water, and a mixture of rock and water of different properties, respectively. In Model-ω-basic we consider the subdomains $\Omega^{(r)}$ and $\Omega^{(w)}$ with a fixed known interface $\partial\Omega^{(r)} \cap \partial\Omega^{(w)}$, while $\Omega^{(w)}$ is partitioned between $\Omega_l^{(w)}$ and $\Omega_i^{(w)}$ separated by the ice-water free boundary. These have heat capacities c_r, c_l, c_i, respectively of rock, liquid water, and ice, shorthand for $c^{(r)}, c_l^{(w)}, c_i^{(w)}$, respectively. Similarly, we have heat conductivities k_r, k_l, k_i. In Model-ω-extended we allow different subdomains $\Omega^{(w,m)}$, $m = 1, \dots N_{WMAT}$ within $\Omega^{(w)}$, but for simplicity we consider only one mineral rock grain type numbered $r = N_{MAT} = N_{WMAT} + 1$.

2.1.3. Scales and periodic geometry. We consider two scales: the Darcy scale and the pore-scale. The Darcy scale quantities depend on the position $x \in \Omega$. The pore-scale variables and quantities depend on $y \in \omega(x)$ within a local REV (Representative Elementary Volume) $\omega(x)$ centered at x. Typically, we assume that the typical quantity $\epsilon_0 = \frac{diam(\omega)}{diam(\Omega)}$ is small, which renders this separation of scales meaningful. We also assume that Ω is made of a large number of statistically nearly identical copies of ω. If they are identical, we call this "the periodicity assumption", and each REV ω is a cube of edge length ϵ in each direction and identical, up to scaling, to a so-called unit cell $\mathcal{Y}$, a cube with volume 1. For some thermal property $v(x)$ varying periodically in Ω with period ϵ, one can then write $v = v(x, y), y = \frac{x}{\epsilon}$. This homogenization Ansatz is well known [43, 22].

At the pore-scale we consider $\omega^{(m)}(x) = \omega(x) \cap \Omega^{(m)}$ and $\omega_p^{(m)}(x) = \omega(x) \cap \Omega_p^{(m)}$ within $\omega(x)$; see Figure 1, and we define the volume fraction $\eta^{(m)}(x) = \frac{|\omega^{(m)}|}{|\omega(x)|}$. In porous media, the rock and water regions $\omega^{(r)}$ and $\omega^{(w)}$, respectively, are most important, and we define the porosity $\eta(x) = \eta^{(w)}(x)$.

For the phase p of material m we define its relative volume fraction $\chi_p^{(m)} = \frac{|\omega_p^{(m)}|}{|\omega^{(m)}|}$ occupied by this phase with respect to the total amount of the material. In particular, we have the (evolving in time) liquid water fraction $\chi_l^{(w)}(x,t) = \frac{|\omega_l^{(w)}(x,t)|}{|\omega^{(w)}(x)|}$. In flow models such volume fractions are usually called "phase saturations". In turn, permafrost literature refers to $\eta\chi_l^{(w)}$ as the "volumetric unfrozen (liquid) water content". We also abbreviate and write $\chi_l = \chi_l^{(w)}$.

2.1.4. Local averages. Since we aim to compare our results with those in the literature, we recall now the local REV volumetric average $\langle \upsilon \rangle(x)$ of some quantity $\upsilon(x,y)$,

$$\langle \upsilon \rangle = \frac{1}{|\omega(x)|} \int_{\omega(x)} \upsilon(x;y)dy. \tag{2.4}$$

The weighted arithmetic (parallel), geometric, and harmonic (series) averages of some property υ which takes a constant value $\upsilon^{(m)}$ in each material are given as

$$\upsilon^A = \langle \upsilon \rangle = \sum_{m=1}^{N_{MAT}} \eta^{(m)} \upsilon^{(m)}; \tag{2.5a}$$

$$\upsilon^G = \Pi_{m=1}^{N_{MAT}} (\upsilon^{(m)})^{\eta^{(m)}}; \tag{2.5b}$$

$$\upsilon^H = \langle 1/\upsilon \rangle^{-1} = \left(\sum_{m=1}^{N_{MAT}} \eta^{(m)} (\upsilon^{(m)})^{-1} \right)^{-1}. \tag{2.5c}$$

These averages are functions of x, since $\omega = \omega(x)$, and each material volume fraction $\eta^{(m)} = \eta^{(m)}(x)$. If material's properties depend on a phase, these definitions are readily extended. In particular, as commonly considered in the applications literature, we consider some property υ with values $\upsilon_r, \upsilon_l, \upsilon_i$ in each $\omega^{(r)}, \omega_l^{(w)}, \omega_i^{(w)}$ lumped together in the "unfrozen" (thawed) and "frozen" material properties found by arithmetic or geometric averaging $\upsilon_u^A = (1-\eta)\upsilon_r + \eta\upsilon_l$, $\upsilon_f^A = (1-\eta)\upsilon_r + \eta\upsilon_i$, and $\upsilon_u^G = \upsilon_r^{(1-\eta)}\upsilon_l^\eta$, $\upsilon_f^G = \upsilon_r^{(1-\eta)}\upsilon_i^\eta$ as follows:

$$\upsilon^A = \langle \upsilon \rangle = \upsilon_r(1-\eta) + \eta(\upsilon_l\chi_l + (1-\chi_l)\upsilon_i) = \upsilon_u^A\chi_l + \upsilon_f^A(1-\chi_l), \tag{2.6a}$$

$$\upsilon^G = \upsilon_r^{1-\eta}(\upsilon_l^{\eta\chi_l}\upsilon_i^{\eta(1-\chi_l)}) = (\upsilon_u^G)^{\chi_l}(\upsilon_f^G)^{1-\chi_l}, \tag{2.6b}$$

$$\upsilon^H = \langle 1/\upsilon \rangle^{-1}. \tag{2.6c}$$

These quantities depend on the phase properties represented by the relative fraction χ_l of the liquid phase.

2.2. Heat conduction in porous medium at the pore-scale. Let Ω represent a porous medium made of rock grains in $\Omega^{(r)}$ and void space filled with water $\Omega^{(w)}$. To describe heat conduction in Ω, we use (2.3) in $\Omega^{(r)}$, and the model for freezing/thawing of water in $\Omega^{(w)}$, coupled by the continuity of temperature and fluxes across the rock-water interface $\Gamma^{(rw)}$. This special case of general heterogeneous Stefan problem described in section 2.2.1 gives Model-ω-basic in section 2.2.2; we extend it to Model-ω-extended to describe the realistic microphysics in section 2.2.3.

2.2.1. Heterogeneous Stefan problem.

Assumption 2.1. We assume that the properties of the materials are piecewise constant in each phase l, i and material m, for example, when m represents rock or water. In particular, $c_l^{(m)}$, $c_i^{(m)}, \theta_*^{(m)}, L^{(m)}, k_l^{(m)}, k_i^{(m)}$ are constants that are specific to the material type (m). We also assume that the interface $\bigcup_{mj} \Gamma^{(mj)}$ between any two materials m, j is fixed in time and perfectly conducting. For well-posedness and physical meaning, we assume that there exist constants $c_{min}, c_{max}, k_{min}, k_{max}$:

$$0 < c_{min} \le c_l^{(m)}, c_i^{(m)} \le c_{max}, \quad 0 < k_{min} \le k_l^{(m)}, k_i^{(m)} \le k_{max}, \quad 0 \le L^{(m)} \text{ for all } m. \tag{2.7}$$

We also assume $\mathcal{T} = (\theta_*^{(m)})_m$ is a nondecreasing sequence. This is done for the convenience of notation for calculations in section 3.2, and does not change any of the physics of the problem.

Now let (2.3) hold in each material subdomain $\Omega^{(m)}$ $m = 1, \dots N_{MAT}$:

$$\partial_t(w) - \nabla \cdot (k^{(m)}(\theta)\nabla\theta)) = f, \quad w \in \alpha^{(m)}(\theta) \text{ in } D(\Omega_T^{(m)})', \tag{2.8a}$$

$$\alpha^{(m)}(\theta) = \begin{cases} c_i^{(m)}(\theta - \theta_*^{(m)}); & \theta < \theta_*^{(m)}, \\ [0, L^{(m)}]; & \theta = \theta_*^{(m)}, \\ c_l^{(m)}(\theta - \theta_*^{(m)}) + L^{(m)}; & \theta > \theta_*^{(m)}. \end{cases} \tag{2.8b}$$

To close the problem, we need some transmission conditions on every interface $\Gamma^{(mj)} = \partial\Omega^{(m)} \cap \partial\Omega^{(j)}$. We assume no thermal resistance which yields continuity of θ as well as of the heat flux

$$\theta^{(m)}|_{\Gamma^{(mj)}} = \theta^{(j)}|_{\Gamma^{(mj)}}; \quad k^{(m)}\nabla\theta^{(m)} \cdot n|_{\Gamma^{(mj)}} = k^{(j)}\nabla\theta^{(j)} \cdot n|_{\Gamma^{(mj)}}. \tag{2.8c}$$

Since the interface $\bigcup_{mj} \Gamma^{(mj)}$ is fixed, we can combine the portions of (2.8) for each material and write these in the sense of distributions over Ω_T analogous to (2.3); see, e.g., [13]. With the material properties variable in $x \in \Omega$ as in (2.8) we have

$$\partial_t(w(x,t)) - \nabla \cdot (k(\theta, x)\nabla\theta) = f \text{ in } D(\Omega_T)'; \, w(x,t) \in \alpha(\theta(x,t), x), \text{ a.e. } x, t. \tag{2.9a}$$

When (2.9a) is supplemented with appropriate boundary and initial conditions

$$\theta(x,t)|_{\partial\Omega_D} = \theta_D(x,t); q \cdot n|_{\partial\Omega\setminus\partial\Omega_D} = 0, \quad w(x,0) = w_{init}(x), x \in \Omega, \tag{2.9b}$$

the well-posedness of (2.9) can be studied. In particular, [60, Cor. 4.1 of Thm 4.1] proves the existence of solution $\theta \in L^2(H^1)$ as a limit of Rothe approximations to a regularized problem, under nonlinear boundary conditions, and provided $w_{init} \in L^\infty$ as well as that each $\Omega^{(m)}$ is a bounded Lipschitz domain. In the multiscale setting there are existence results in [73] for (2.9); we recall their statement in section 3.1.1.

2.2.2. Model-ω-basic at the pore-scale. We consider a special case of heterogeneous Stefan problem (2.8). In $\Omega^{(w)}$ we have $\alpha^{(w)}$ given as in (2.8b) with the properties of bulk water. In $\Omega^{(r)}$ we have no phase change within the range of temperatures of interest but we can use the definition (2.8b) setting

$$L^{(r)} = 0, c_l^{(r)} = c_i^{(r)} = c_r, k_l^{(r)} = k_i^{(r)} = k_r, \theta_*^{(r)} = \theta_*^{(w)}. \tag{2.10}$$

The choice $\theta_*^{(r)} = \theta_*^{(w)}$ has no physical meaning and is made for the convenience of notation in the forthcoming upscaling formulas. On the interface $\Gamma^{(rw)} = \partial\Omega^{(r)} \cap \partial\Omega^{(w)}$ we adopt (2.8c).

The relationships $(\alpha^{(m)})_m$ in this Model-ω-basic will be upscaled to α_{eff} in Model-Ω-basic in section 4.1.1. Conductivity $(k^{(m)})_m$ will be upscaled to k_{eff} in section 4.2.

2.2.3. Model-ω-extended at the pore-scale. The physics of freezing of the pore water $\Omega^{(w)}$ is not the same as in the bulk water, except perhaps in large pores. This microphysics is crucial to obtain agreement of upscaled models in section 4.1.2 with the empirical models.

The energy landscape at the fluid-rock interfaces is known to be very complex [1, 56, 28]. In particular, the microscale thermodynamics of confined regions involves

the phenomena of "thermal regelation" and "premelting" caused by the interactions between mineral grains and those of water molecules. As a consequence, at subfreezing temperatures, small amounts of liquid coexist in equilibrium with solid ice because of the wetting interactions and surface-energy effects. These are best interpreted with the theories of adsorption involving van der Waals and other forces, rather than with focus only on thermal conduction. In models and experiments, there are also consideration of flat or nonflat soil-water interfaces, connected or disconnected liquid film, and the relative significance of the adsorptive versus capillary forces. These important microphysics phenomena result in two interconnected features: (i) a depression of freezing temperature prominent in small pores, and (ii) the presence of a thin film of (undercooled) water around the grains.

In this paper, we focus on (i) which is critical for thermal models since it leads to the long-tailed behavior of $\alpha^P(\theta)$ at the Darcy scale, discussed later in section 2.3. We recall the Gibbs–Thomson law which provides the formula for the depression in phase change temperature $\Delta\theta_* = -\frac{2\sigma\theta_*}{RL}$, where σ[J/m^2] is the surface-tension coefficient, θ_*[K] is the phase change temperature, and R[m] radius of the curvature, and the dependence of $\Delta\theta_*$ on R comes from that for the curvature $\kappa = \frac{1}{R}$; see [18, p. 50, eq. (2.2.6)], and [72, eq. (IV.2.2,3.1)]. We note in passing that the Gibbs–Thomson relationship is related to the Young–Laplace relationship in capillary phenomena [4, p. 257–259], [29, p. 48–55], which, in turn, can be used to estimate the pore radius. Estimates of the pore radius R are available from the applications literature as well as from X-ray micro-CT images [48, 49, 50, 59]. Since $\theta_*^{(w)} = 0$[°C], we postulate

$$\theta_*^{(w)} = \Delta\theta_*^{(w)} = -\frac{F^{GT}}{R}[^\circ\mathrm{C}], \tag{2.11}$$

where F^{GT} must be chosen. In particular, we can set $F^{GT} = F_0^{GT} = \frac{2\sigma\theta_*[\mathrm{K}]}{L}$.

Our idea is to set up Model-ω-extended in which the pore water domain is partitioned to a collection of pore subdomains, each associated with some characteristic radius size R, for which an individual freezing temperature is calculated with (2.11). This Model-ω-extended is made precise and upscaled to Model-Ω-extended in section 4.1.2.

Remark 2.1. For water in porous medium $\theta_*^{(w)} = 273.15$[K], $\sigma \approx 7.536 \times 10^{-2}$[J/m^2], (surface tension coefficient) [72.99, p. 99], and L is as in Table 2. We get $F_0^{GT} = 1.2 \times 10^{-7}$ [m°C]. If $F^{GT} = F_0^{GT}$, then to lower the temperature with (2.11) by $1°C$, we must have a small enough pore radius $R \approx R_0 = 10^{-1}$ [m] $= 0.1$ [μm]. Such pores are present in realistic porous media [21, 29]. To apply (2.11) in multiscale setting we will consider scaling of F^{GT} developed in section 4.1.2.

Remark 2.2. To accommodate (ii), one can introduce an additional type of subdomain $\omega^{(ul)}$ containing thin (nano-) film of undercooled water around each grain for which we set $\theta_*^{(ul)}$ to be far below the freezing temperatures of any of the pores. However, since the volume fraction $\eta^{(ul)}$ is very small, its influence on the Darcy scale thermal parameters can be ignored. On the other hand, the impact of $\omega^{(ul)}$ on the flow parameters is substantial but these are outside the present scope.

The relationships $(\alpha^{(m)})_m$ in this Model-ω-extended will be upscaled to α_{eff} in Model-Ω-extended in section 4.1.2 Conductivity $(k^{(m)})_m$ will be upscaled to k_{eff} as shown in section 4.2.

2.3. Model-Ω-empirical for heat conduction at the Darcy scale. There is considerable literature devoted to permafrost models in civil, petroleum, and geotech-

nical engineering, hydrology, soil science, and more recently, in computational environmental climate models; see some representative papers in [20, 75, 1, 28, 67, 57, 24, 40, 23]. The thermal Model-Ω-empirical at the Darcy scale specializes (1.1) to

$$\partial_t w - \nabla \cdot (k^P \nabla \theta) = f;\ w(x,t) = \alpha^P(\theta). \tag{2.12}$$

The single valued experimentally calibrated formulas for $\alpha^P(\theta)$ as well as $k^P(\theta)$ treat soil as a single material while they incorporate c_r, c_l, c_i, L and k_r, k_l, k_i, the porosity $\eta(x)$, and the key property, the liquid (unfrozen) volume fraction $\chi_l^P(\theta)$, also known as SFC (Soil Freezing Curve), given in section 2.3.1. Once $\chi_l^P(\theta)$ is selected, $\alpha^P(\theta)$ is found similarly to (2.1)

$$w(\theta) = \alpha^P(\theta) = \int_{\theta_*}^{\theta} c(v)dv + L\eta\chi_l^P(\theta);\quad c(v) = c_u\chi_l^P(v) + c_f(1-\chi_l^P(v)) \tag{2.13}$$

with c_u, c_f are the (porosity weighted) heat capacities of the "unfrozen" and "frozen" soil, defined as before (2.5). The formula (2.13) requires an integral of a given nonlinear $\chi_l^P(v)$.

Remark 2.3. The models for $\chi_l^P = \chi_l^P(\theta)$ assume instantaneous local equilibrium, i.e., that the liquid fraction $\chi_l^P(x,t)$ responds instantaneously to the changes in temperature $\theta(x,t)$; equivalently, they assume that (some amount of) the ice forms instantly when the temperatures drop. This not entirely realistic feature ignores the presence of undercooled water, the mechanisms of nucleation, as well as the nonnegligible scale effect. We refer to the discussions of related experimental difficulties in [28], observations of apparent hysteresis in $\chi_l^P(\theta)$ in [57] and to theoretical relevant work on hysteresis including [32, 44, 46]. However, an in-depth discussion of nonequilibrium models is outside our scope.

2.3.1. Empirical models for the soil freezing curve χ_l^P leading to α^P. The SFC models for $\chi_l^P(\theta)$ are calibrated from empirical measurements, and the algebraic formulas vary from power models to exponential to blended models which fit best particular types of soils (clay, silt, sand); see, e.g., [75, 42, 38, 30, 27, 57], as well as a recent through review in [28]. Some works relate SFC to capillary phenomena and the Clausius–Clapeyron equation; those efforts may be relevant for the flow models, but are not directly relevant to our scope.

All the SFC models share common qualitative behavior, and, in particular, (a) have a long-tailed behavior as $\theta\downarrow$. Some works postulate $\lim_{\theta\to-\infty}\chi_l^P(\theta) = \chi_{res} > 0$, and some $\chi_{res} = 0$. In addition, (b) some SFCs are discontinuous at $\theta = 0$ so that $\lim_{\theta\to 0^-}\chi_l^P(\theta) = \chi_0 \neq 1 = \chi_l^P(\theta)|_{\theta>0}$. This lack of continuity if $\chi_0 \neq 1$ presents challenges to computations, a feature noted in [26]. In turn, [28] considers the smoothness mandatory and requires $\chi_0 = 1$, while some choose parameters for which $\chi_0 = 1$; see, e.g., [78, 33]. In this paper we adapt SFC from the literature to ensure continuity at $\theta = \theta_*$,

$$\chi_l^P(\theta) = \begin{cases} 1; & \theta \geq \theta_*; \\ \Upsilon^P; & \theta < \theta_* \end{cases} \tag{2.14}$$

and consider $\chi_l^L(\theta), \chi_l^W(\theta), \chi_l^M(\theta)$ from [34, 75, 38], respectively, with the symbols L, W, M chosen according to the original author's names, $\Upsilon^L = |\theta_*|^b|\theta|^{-b}$, $\Upsilon^W = \chi_{res} + (1-\chi_{res})(\frac{b}{b-\theta+\theta_*})^4$, $\Upsilon^M = \chi_{res} + (1-\chi_{res})e^{b(\theta-\theta_*)}$. We illustrate these in Figure 2 along with the plots of the corresponding $\alpha^P(\theta)$ calculated with (2.13). Additional data on the parameters typical for $\chi_l^{model}(\theta)$ is given in Table 8 ; see also soil-specific data available in [1, 57] and [2, 28].

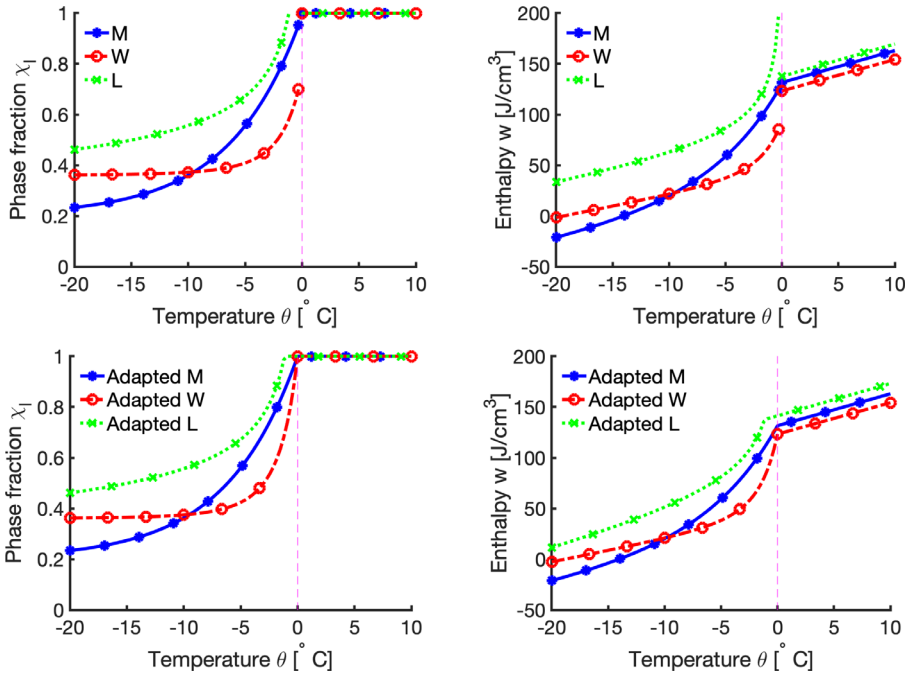

FIG. 2. *Plot of the Darcy-scale relationships* $\chi_l^P(\theta)$ *(left) and* $w = \alpha^P(\theta)$ *(right) used in Model-*Ω*-empirical for clay using the parametric models* $\chi_l^{model}(\theta)$ *with model* $= L, W, M$ *given by* (2.14) *from section* 2.3.1*, and with data from Table* 7*. The original relationships (top) may be discontinuous, the adapted (continuous at* $\theta = 0$*) are on the bottom.*

2.3.2. Empirical models for heat conductivity $k^P(\theta)$ at the Darcy scale. Once a particular χ_l^P is selected as in section 2.3.1, the Model-Ω-empirical uses simple weighted average expressions for $k^P = k^P(\chi_l^P(\theta))$ based on (2.6),

$$k^A = k_u^A \chi_l^P + k_f^A (1 - \chi_l^P);\ k_u^A = (1-\eta)k_r + \eta k_l,\ k_f^A = (1-\eta)k_r + \eta k_i, \tag{2.15a}$$

$$k^G = (k_u^G)^{\chi_l^P} (k_f^G)^{(1-\chi_l^P)};\ k_u^G = k_l^\eta k_r^{1-\eta};\ k_f^G = k_i^\eta k_r^{1-\eta}, \tag{2.15b}$$

$$k^H = \langle 1/k(\cdot) \rangle. \tag{2.15c}$$

Each of k^A, k^G, k^H is a function of $x, t, \theta(x,t)$ since $\eta = \eta(x)$ and $\chi_l^P = \chi_l^P(\theta(x,t), x)$.

In particular, k^G is used in [42, 23, 38, 78], and [1, Figures 2–27], and k^A is used in [33]. In turn, k^H do not seem to be known or used in geophysics. In more general context, arithmetic and harmonic averaging correspond to composite materials arranged "in parallel" or "in series".

We emphasize that the above formulas rely on the average liquid water content χ_l^P; they do not account for the specific partition of the geometry of $\omega^{(w)}$ into $\omega_l^{(w)}$ and $\omega_i^{(w)}$. In contrast, we address this geometrical aspect when calculating k_{eff} in section 4.2 which we compare to the averages given by (2.15).

3. Upscaling Model-ω to Model-Ω. In this section we describe how to bridge between the pore-scale and the Darcy scale for the thermal models of permafrost. At the pore-scale permafrost is a composite medium described by Model-ω (2.8) written here as an ϵ-model for the geometry from section 2.1.3,

$$\partial_t(w^\epsilon(x,y,t)) - \nabla\cdot(k(\theta^\epsilon,x,y)\nabla\theta^\epsilon) = f \text{ in } D(\Omega_T)';$$
$$w^\epsilon(x,y,t) \in \alpha(\theta^\epsilon(x,y,t),x), \text{ a.e. } x\in\Omega, y\in\mathcal{Y}, t>0. \tag{3.1}$$

At the Darcy scale we derive effective properties α_{eff} and k_{eff} for Model-Ω describing $(\bar\theta,\bar w)$,

$$\partial_t(\bar w) - \nabla\cdot(k_{eff}(\bar\theta)\nabla\bar\theta) = f, \quad \bar w \in \alpha_{eff}(\bar\theta) \text{ in } D(\Omega_T)', \tag{3.2}$$

which we aim to compare to the Model-ω-empirical (2.12) from section 2.3.

We aim to upscale Model-ω to Model-Ω, and start with the theoretical background in section 3.1. Without the phase change, upscaling the thermal properties is an easy task. In particular, it is well known that $w^\epsilon(x,y,t) = c\theta^\epsilon(x,y,t)$ in (3.1) is well approximated asymptotically by $\bar w = c_{eff}\bar\theta$ with $c_{eff} = \langle c\rangle$. In turn, k_{eff} can be calculated by well known formulas involving an auxiliary elliptic boundary value problem on the cell. The process to find c_{eff}, k_{eff} is well known; see, e.g., [43, 22]. However, the freezing and thawing scenarios in permafrost soils requires handling the nonlinear $k(\theta)$ and multivalued relationships $w\in\alpha(\theta)$; in this paper we follow the rigorous theory in [13, 73]. In a more general context, for homogenization of nonlinear flow models when multiple phases and/or additional processes such as precipitation or biofilm growth are involved, we refer to, e.g., [45, 49, 7, 55].

In section 3.2 we derive the upscaled relationships $\alpha_{eff}(\theta)$. First, in section 4.1.1 we work with Model-ω-basic, but the corresponding upscaled α_{eff} in Model-Ω-basic is qualitatively different from α^P in Model-Ω-empirical. In section 4.1.2 we therefore propose a new Model-ω-extended to include additional microphysics; after upscaling to Model-Ω-extended, we get α_{eff} similar to α^P in some Model-Ω-empirical.

In section 4.2 we discuss $k_{eff}(\theta)$. In some circumstances we find that the rigorously derived coarse-scale models for k_{eff} are close to simple averages given for k^P by (2.15). In general, however, these averages are not accurate while the general formulas depend on the local geometry; we follow up with recommendations on most useful (also reduced) approximations $\widetilde{k_{eff}}$, guided by the pore-scale examples.

3.1. Background. The mathematical theory of homogenization for PDEs in composite materials is very well established; we refer to the abundant theory in the classical as well as modern expositions in [43, 62, 16]. In geosciences and specifically porous media, the derivation of effective parameters and models can proceed within the rigors of homogenization theory and/or the algorithms of numerical upscaling and/or the framework of volume averaging; these are well explained, e.g., in [22, 4]. While the multiscale efforts originally focused on the flow properties from the Darcy to the field scale, upscaling from the pore- to the Darcy scale has recently drawn considerable attention, including for the flow [69, 47, 48, 49], and for other and coupled processes [19, 7, 8]. These works provide selected perspectives on modeling in porous media which inform research in this paper. Some of these, as well as the work deriving from Heterogeneous Multiscale Method (HMM) in [10] couple the scales dynamically, i.e., HMM models probe the Model-ω whenever data for Model-Ω is needed at grid-points covering Ω, and two-scale models maintain the implicit connection between the micro- and macromodel. In this work we follow [73] who define both two-scale as well as the effective approaches.

For nonlinear and coupled problems, there are additional complications which one must address, since now the upscaled relationships may be functions rather than constants. Specifically, such relationships arise in the work on homogenization of nonlinear models of phase transitions outlined in [73] and earlier work in [13] specifically on a simplified Stefan problem form the theoretical foundations for this work.

First, make a rigorously justified and practical connection between the pore- and the Darcy scale models, deriving effective properties rather than the two-scale approaches. The large separation of scales between the pore-scale of [μm] and the Darcy scale of [cm]–[m] of empirical models combined with the large uncertainty of the geometry at the pore-scale [49, 64, 50] as well as with the specifics of freezing/thawing in micropores suggest that the two-scale simulation may not be feasible for permafrost.

Second, we work with the "actual" physical size of the pore-scale region $y \in \omega(x)$ as well as with the mathematically idealized unit cell $\mathcal{Y}$. We also maintain a realistic connection to the scale-dependent microphysics at the grain-water interfaces.

Third, we embrace the enormous complexity of realistic pore geometries. In fact, the REV ω must contain a large variety of pore sizes so that the effective relationships compare well to those found empirically. This aspect can be combined eventually with the strategy in [50] to guide the construction of surrogate effective models built offline.

3.1.1. Theory for upscaling nonlinear heat equation with phase change. We now recall the theory including notation, assumptions, and main results derived in [73] which employs traditional homogenization applied to (2.9); we provide our corresponding notation in brackets.

The unknowns in [73] are w, u, q (we use w, θ, q), with the freezing temperatures $u_*(x)$ $[\theta_*(x)]$. The constitutive enthalpy-temperature relationship is $w \in \partial\psi(u, x, y)$ $[w \in \alpha(\theta, x, y) = \partial\psi(\theta, x, y)]$, and its primitive $\psi(v, x, y)$ is assumed [73, eqs. (2.28), (2.29), (3.18)] proper, strictly convex lower semicontinuous and bounded from below by a quadratic a.e. (x, y) (these hold for ψ in (2.2)). In addition, [73, eq. (3.1)] assumes $w \in \partial\psi(v, x, y)$ is bilaterally affine bounded $c_1|v| + h_1(x) \le |w| \le \tilde{c}_1|v| + \tilde{h}_1(x)$ (these hold due to Assumption 2.1) for some positive $c_1, \tilde{c}_1$ and $h_1, \tilde{h}_1 \in L^1(\Omega)$. The flux-temperature relationship in [73, eqs. (2.36)–(2.37) and (3.2)–(3.4)] is $q = q(\nabla u, u, x, y, t)$ which must be affine bounded (we consider $q = -k(\theta, x, y)\nabla\theta$ linear in $\nabla\theta$ for which the bound and properties hold due to Assumption 2.1).

The boundary conditions in [73] include those on the Dirichlet portion $\partial\Omega_D$ of $\partial\Omega$ which is assumed to have nonzero measure (this agrees with (2.9b)). The source f in [73] is allowed to be nonlinear in u and satisfy some bounds. (We only consider the source $f \in L^2(V')$, with $V = \{v \in H^1(\Omega) : v|_{\partial\Omega_D} = 0\}$).

For homogenization to a two-scale problem and upscaling to a coarse problem, [73] considers dependence of data on $x, y = \frac{x}{\epsilon}$ to be periodic in $y \in \mathcal{Y}$ with a unit measure cell $\mathcal{Y}$. The averages over $\mathcal{Y}$ are denoted by $\hat{p}$, we use $\langle p \rangle$.

We recall the theory in Remark 7.1 in the appendix. We summarize now how it applies to (2.9).

PROPOSITION 3.1 (adapted from [73, Thms. 4.1 and 5.4)]. *There exists a family of ϵ-solutions $(u^\epsilon, w^\epsilon, q^\epsilon)$ of (2.9) which are bounded uniformly in ϵ in the norms in $L^2(H^1)$ and $L^\infty(L^2) \cap H^1(V')$, and $(L^2(\Omega_T))^d$, respectively. Their asymptotic limits satisfy the problem*

$$\partial_t \bar{w} + \nabla_x \cdot \bar{q} = \langle f \rangle, \quad \bar{w} \in \alpha_{eff}(\bar{\theta}) = \partial\psi_{eff}(\bar{\theta}), \quad \bar{q} = -k_{eff}(\bar{\theta})\nabla_x\bar{\theta} \text{ in } D'(\Omega_T), \tag{3.3}$$

where $\psi_{eff}(v) = \langle \psi(v, \cdot) \rangle$, and where

$$k_{eff}(v) = (k_{eff,ij})_{ij}; \ k_{eff,ij} = \langle k(v; y)(\delta_{ij} + \partial_i \xi_j) \rangle \tag{3.4a}$$

is found via the corrections $(\xi_j)_{j=1}^d$ which solve the auxiliary periodic elliptic problem

$$-\nabla \cdot (k(\bar{u}, y)(e_j + \nabla_y \xi_j)) = 0; \ \xi_j \text{ periodic on } \mathcal{Y}. \tag{3.4b}$$

Remark 3.1. The result in Proposition 3.1 from [73] generalizes that in [13] for a simpler model with $N_{MAT} = 2$ in which the conductivities are constant in each material and phase independent. In this simplified case uniqueness and regularity of the temperature in $H^1(L^2) \cap L^\infty(V)$ stronger than only $L^2(H^1)$ as in [73] are obtained, and homogenization is carried out. We note that in [13] the transmission conditions identical to (2.8c) which are assumed to be rigid and perfectly conducting are explicitly stated.

In sections 3.2 and 3.3 we identify α_{eff}, k_{eff}, respectively, and their reasonable approximations.

3.2. Finding $\alpha_{eff} = \partial\langle\psi\rangle$ for Model-Ω-effective from Proposition 3.1. We now provide general calculations for heterogeneous Stefan problem (2.8) with any $N_{MAT} > 1$. Assume that the domain Ω is made of N_{MAT} materials arranged in periodic cells $\omega(x)$, with $\omega^{(m)}(x) = \omega(x) \cap \Omega^{(m)}$, $m = 1, \dots N_{MAT}$. The heat properties are material specific and piecewise constant: each $\alpha^{(m)}(\theta)$ is parameterized by $c_l^{(m)}, c_i^{(m)}$, and $L^{(m)}$ as well as $\theta_*^{(m)}$ as in Assumption 2.1. For each material m we have a formula similar to (2.2) for the primitive of $\alpha^{(m)}$,

$$\psi(\theta; y)|_{\omega^{(m)}} = \begin{cases} \frac{c_i^{(m)}}{2}(\theta - \theta_*{}^{(m)})^2, & \theta < \theta_*^{(m)}, \\ \frac{c_l^{(m)}}{2}(\theta - \theta_*{}^{(m)})^2 + L^{(m)}(\theta - \theta_*^{(m)}), & \theta \geq \theta_*^{(m)}. \end{cases} \tag{3.5}$$

With this set-up we apply Proposition 3.1.

PROPOSITION 3.2. *Let ψ be given by* (3.5)*. Then*

$$\alpha_{eff}(\theta) = \partial\psi_{eff}(\theta) = \sum_{m=1}^{N_{MAT}} \eta^{(m)} \partial\psi^{(m)}(\theta) = \sum_{m=1}^{N_{MAT}} \eta^{(m)} \alpha^{(m)}(\theta) \tag{3.6}$$

is a piecewise linear multivalued graph defined as follows:

$$\begin{aligned} \partial\psi_{eff}(\theta)|_{(\theta_*^{(m-1)}, \theta_*^{(m)})} = &\sum_{k=m}^{N_{MAT}} \eta^{(k)} c_i^{(k)} (\theta - \theta_*^{(k)}) + \sum_{k=1}^{m-1} \eta^{(k)} c_l^{(k)} (\theta - \theta_*^{(k)}) \\ &+ \sum_{k=1}^{m-1} \eta^{(k)} L^{(k)} \mathcal{H}(\theta - \theta_*^{(k)}). \end{aligned} \tag{3.7a}$$

In particular, for $\theta < \theta_*^{(1)}$, the formula gives $\partial\psi_{eff}(\theta) = \sum_{k=1}^{N_{MAT}} \eta^{(k)} c_i^{(k)} (\theta - \theta_*^{(k)})$. In turn, for $\theta > \theta_*^{(N_{MAT})}$, we get $\sum_{k=1}^{N_{MAT}} \eta^{(k)} c_l^{(k)} (\theta - \theta_*^{(k)}) + \sum_{k=1}^{N_{MAT}} \eta^{(k)} L^{(k)} H(\theta - \theta_*^{(k)})$. In addition, at each $\theta = \theta_*^{(m)}$, the graph $\partial\psi$ is multivalued, with its jump from left to right given by

$$[\partial\psi_{eff}]_{\theta_*^{(m)}} = \eta^{(m)} L^{(m)}. \tag{3.7b}$$

Proof. The proof is by algebraic calculations and taking subdifferentials. We calculate

$$\psi_{eff}(\theta) = \int_{\mathcal{Y}} \psi(\theta, y) dy = \sum_m \int_{\mathcal{Y}^{(m)}} \psi(\theta, y) dy = \sum_m \eta^{(m)} \psi^{(m)}(\theta). \tag{3.8}$$

Next, we take its subdifferential with respect to θ and get (3.6) also as a volumetric average. The details of (3.7) follow easily; we outline the calculation for $N_{MAT} = 2$;

an extension to the case $N_{MAT} > 2$ is tedious but immediate. We recall the expression (3.5) for $\psi^{(m)}(\theta)$, and see that

$$\partial\psi^{(m)}(\theta) = \alpha^{(m)}(\theta) = \begin{cases} c_i^{(m)}(\theta - \theta_*^{(m)}); & \theta < \theta_*^{(m)}, \\ L^{(m)}\chi^{(m)}(\theta) \in [0, L^{(m)}]; & \theta = \theta_*^{(m)}, \\ c_l^{(m)}(\theta - \theta_*{}^{(m)}) + L^{(m)}; & \theta > \theta_*^{(m)} \end{cases} \tag{3.9}$$

is piecewise linear, with constant slopes $c_i^{(m)}$ for $\theta < \theta_*^{(m)}$, and $c_l^{(m)}$ for $\theta > \theta_*^{(m)}$. At $\theta = \theta_*^{(m)}$ $\alpha^{(m)}$ is multivalued with values in $[0, L^{(m)}]$, i.e., the graph $\alpha^{(m)}$ takes a jump of $L^{(m)}$.

We next characterize the weighted average $\partial\psi_{eff} = \eta^{(1)}\partial\psi^{(1)}(\theta) + \eta^{(2)}\partial\psi^{(2)}(\theta)$. We have either (i) $\theta_*^{(1)} = \theta_*^{(2)}$ or (ii) $\theta_*^{(1)} < \theta_*^{(2)}$. In case (i) both materials undergo phase change at the same temperature $\theta = \theta_*^{(1)} = \theta_*^{(2)}$ at which their properties change from solid (ice) to liquid, thus for $\theta < \theta_*^{(1)}$ we have the slope of α_{eff} equal to $c_{eff} = \eta^{(1)}c_i^{(1)} + \eta^{(2)}c_i^{(2)}$, and for $\theta > \theta_*^{(1)}$, $c_{eff} = \eta^{(1)}c_l^{(1)} + \eta^{(2)}c_l^{(2)}$. The jump of $\partial\psi_{eff}$ at $\theta = \theta_*^{(1)} = \theta_*^{(2)}$ is $\eta^{(1)}L^{(1)} + \eta^{(2)}L^{(2)}$.

In case (ii) we consider first some θ not equal to any of $\theta_*^{(m)}$. For $\theta < \theta_*^{(1)}$, we have

$$\partial\psi_{eff}(\theta) = \eta^{(1)}c_i^{(1)}(\theta - \theta_*^{(1)}) + \eta^{(2)}c_i^{(2)}(\theta - \theta_*^{(2)}).$$

For $\theta_*^{(1)} < \theta < \theta_*^{(2)}$, we have

$$\partial\psi_{eff}(\theta) = \eta^{(1)}c_l^{(1)}(\theta - \theta_*^{(1)}) + \eta^{(1)}L^{(1)} + \eta^{(2)}c_i^{(2)}(\theta - \theta_*^{(2)}).$$

Lastly for $\theta > \theta_*^{(2)}$, we have

$$\partial\psi_{eff}(\theta) = \eta^{(1)}c_l^{(1)}(\theta - \theta_*^{(1)}) + \eta^{(1)}L^{(1)} + \eta^{(2)}c_l^{(2)}(\theta - \theta_*^{(2)}) + \eta^{(2)}L^{(2)}.$$

Considering next $\theta = \theta_*^{(1)}$, we see that $\partial\psi_{eff}(\theta_*^{(1)}) = \eta^{(1)}L^{(1)}\mathcal{H}(\theta - \theta_*^{(1)})$ takes a jump of magnitude $\eta^{(1)}L^{(1)}$. Similarly, at $\theta = \theta_*^{(2)}$ the jump of $\partial\psi_{eff}(\theta_*^{(2)})$ has the magnitude $\eta^{(2)}L^{(2)}$.

The extension to $N_{MAT} > 2$ completes the proof. ∎

Next, we interpret α_{eff} derived in Proposition 3.2 as having a "regular" and "singular" part; the latter associated with the effective volume fraction $\chi_{eff}(\theta)$ which depends only on the data in

$$\mathcal{D} = \left(\theta_*^{(m)}, \eta^{(m)}\right)_{m=1}^{N_{MAT}}. \tag{3.10}$$

COROLLARY 3.1. *The formula* (3.7) *from Proposition* 3.2 *can be decomposed into regular (continuous piecewise linear part $\mathcal{C}_{eff}(\theta)$) and singular (multivalued) parts*

$$\alpha_{eff}(\theta) = \partial\psi_{eff}(\theta) = \mathcal{C}_{eff}(\theta) + \mathcal{L}_{eff}(\theta)\chi_{eff}(\theta). \tag{3.11a}$$

Here $\mathcal{C}_{eff}(\theta)$ is given by

$$\mathcal{C}_{eff}(\theta)|_{[\theta_*^{(m-1)}, \theta_*^{(m)}]} = \sum_{k=1}^{m-1} \eta^{(k)}c_l^{(k)}(\theta - \theta_*^{(k)}) + \sum_{k=m}^{N_{MAT}} \eta^{(k)}c_i^{(k)}(\theta - \theta_*^{(k)}), \tag{3.11b}$$

with the (variable) slopes $c_{eff}(\theta)$ *given by*

$$c_{eff}(\theta)\big|_{(\theta_*^{(m-1)},\theta_*^{(m)})} = \sum_{k=1}^{m-1} \eta^{(k)} c_l^{(k)} + \sum_{k=m}^{N_{MAT}} \eta^{(k)} c_i^{(k)}. \tag{3.11c}$$

The multivalued $\mathcal{L}_{eff}(\theta)\chi_{eff}(\theta)$ *portion of* (3.11a) *is*

$$\mathcal{L}_{eff}(\theta)\chi_{eff}(\theta) = \sum_{k=1}^{N_{MAT}} \eta^{(k)} L^{(k)} \mathcal{H}(\theta - \theta_*^{(k)}). \tag{3.11d}$$

The effective liquid fraction is the average $\chi_{eff}(\theta) = \sum_{m=1}^{N_{MAT}} \eta^{(m)} \mathcal{H}(\theta - \theta_*^{(m)})$ *multivalued at* $\theta_*^{(m)}$*:*

$$\chi_{eff}(\theta) = \begin{cases} 0, & \theta \in (-\infty, \theta_*^{(1)}), \\ \eta^{(1)}, & \theta_*^{(1)} < \theta < \theta_*^{(2)}, \\ \dots & \\ \displaystyle\sum_{k=1}^{m-1} \eta^{(k)}, & \theta_*^{(m-1)} < \theta < \theta_*^{(m)}, \\ \dots & \\ 1, & \theta_*^{(N_{MAT})} < \theta, \end{cases} \tag{3.11e}$$

$$\chi_{eff}(\theta_*^{(m)}) = \left[\sum_{k=1}^{m-1} \eta^{(k)}, \sum_{k=1}^{m} \eta^{(k)} \right].$$

The weighted average latent heat $\mathcal{L}_{eff}(\theta) = (\sum_{k=1}^{m-1} \eta^{(k)} L^{(k)} \mathcal{H}(\theta - \theta_*^{(k)}))(\sum_{k=1}^{m-1} \eta^{(k)})^{-1}$ *is given as*

$$\mathcal{L}_{eff}(\theta)\big|_{[\theta_*^{(m-1)},\theta_*^{(m)})} = \begin{cases} 0, & \theta \in (-\infty, \theta_*^{(1)}), \\ L^{(1)}, & \theta_*^{(1)} \le \theta < \theta_*^{(2)}, \\ \dots & \\ \dfrac{\displaystyle\sum_{k=1}^{m-1} \eta^{(k)} L^{(k)}}{\sum_{k=1}^{m-1} \eta^{(k)}}, & \theta_*^{(m-1)} \le \theta < \theta_*^{(m)}, \\ \dots & \\ \displaystyle\sum_{k=1}^{N_{MAT}} \eta^{(k)} L^{(k)}, & \theta_*^{(N_{MAT})} \le \theta. \end{cases} \tag{3.11f}$$

Proof. The proof follows by algebraic calculations. First, we note that $\mathcal{C}_{eff}$ represents the first two terms on the right-hand side of (3.7), and that the third and last term of this equation form the right-hand side of (3.11d), modified by extending the sum to all $m = 1, \dots N_{MAT}$. But when $\theta < \theta_*^{(m)}$ for some m, all the terms $\mathcal{H}(\theta - \theta_*^{(k)})$ for $k > m$ are zero. Similar extension applies in (3.11e).

Since $\mathcal{C}_{eff}$ is clearly piecewise linear, we need only verify its continuity, say, at $\theta_*^{(m-1)}$ when $m = 2, \dots N_{MAT} + 1$, where the formula in (3.11b) changes from interval $(\theta_*^{(m-2)}, \theta_*^{(m-1)})$ to $(\theta_*^{(m-1)}, \theta_*^{(m)})$, and shifts the term involving $c_i^{(m-1)}$ to $c_l^{(m-1)}$ from one sum to the other. Since the term involves $\theta - \theta_*^{(m-1)}$, which equals 0 at $\theta_*^{(m-1)}$,

each $(\theta - \theta_*^{(m-1)})$ is piecewise linear continuous on $\mathbb{R}$, and therefore, their linear combination $\mathcal{C}_{eff}$ which is continuous.

To verify (3.11f), we match the expressions on its right-hand side for a given $\theta \in (\theta_*^{(m-1)}, \theta_*^{(m)})$ with (3.11d). We also confirm the jumps at $\theta = \theta_*^{(m-1)}$ where the graph is multivalued. ∎

COROLLARY 3.2. *We summarize the practical steps following Proposition* 3.2 *and Corollary* 3.1 *to get* $\alpha_{eff}(\theta)$. *These do not require explicit calculation of* $\psi_{eff}(\theta)$.

(STEP 1*) Arrange the materials with nondecreasing* θ_*.

(STEP 2*) Calculate the regular portion* $\mathcal{C}_{eff}(\theta)$ *of* $\alpha_{eff}(\theta)$ *with* (3.11b).

(STEP 3*) Calculate the effective* $\chi_{eff}(\theta)$ *with* (3.11e).

(STEP 4*) Calculate the effective* $L_{eff}(\theta)$ *with* (3.11f).

(STEP 5*) Assemble* $\alpha_{eff}(\theta)$ *from STEP* 2*–STEP* 4 *with formula* (3.11a).

Example 3.1 (academic example illustrating the steps of upscaling). Consider the data in Table 3 for $N_{MAT} = 3$ hypothetical materials, and pursue upscaling with STEPS 2–5. The plots in Figure 3 illustrate the process. The total amount of latent heat required to melt all the solid phase in the three materials equals the weighted average $3 * \frac{5}{15} + 5 * \frac{6}{15} + 1 * \frac{4}{15} = 1 + 2 + \frac{4}{15} = 3\frac{4}{15}$ of the different latent heats $(L^{(m)})_m$ reflected as the jump of L_{eff} from far left to far right. We also see a jump in the graph of $\alpha_{eff}(\theta)$ at each of the three freezing temperatures for the three materials.

We apply Corollary 3.2 for upscaling $(\alpha^{(m)})_m$ to α_{eff} from the pore- to the Darcy scale in section 4.1.

3.3. Upscaling $(k^{(m)})_m$ to k_{eff}. We now revisit the definition of k_{eff} in (3.4). A useful approximation $\widetilde{k_{eff}}$ to k_{eff} can be found by averaging $\tilde{\xi}_i$ instead of ξ_i, where $\tilde{\xi}_j$ solves a mixed Dirichlet–Neumann problem instead of periodic problem. This latter problem is frequently used by researchers working with software for elliptic boundary value problem solvers which do not allow period boundary conditions, but allow a mixture of Dirichlet and Neumann conditions. These two approaches are well compared in [15], where a strong case is made for flow problems that $\widetilde{k_{eff}}$ is a poor approximation for k_{eff} if either the geometry of composite REV cell $\omega(x)$ has a strong non-axi-symmetric trend, and/or if the individual conductivities differ by orders of magnitude. For the thermal applications considered here we find, however, that $\widetilde{k_{eff}}$ may be adequately accurate.

We compare $\widetilde{k_{eff}}$ as well as averages (2.15) to k_{eff} for the pore- to the Darcy scale in section 4.2.

4. Results of upscaling Model-ω to Model-Ω. Now we apply the theoretical derivations from section 3 to upscaling from the pore-scale to the Darcy scale: we discuss α_{eff} first in section 4.1. For Model-ω-basic, these do not compare well to the relationships α^P, k^P used in Model-Ω-empirical. Therefore, we extend the simple Model-ω-basic to Model-ω-extended, and improve the agreement after upscaling to Model-Ω-extended with empirical data.

TABLE 3
Thermal data for Example 3.1.

Material	$c_i^{(m)} \vert c_l^{(m)}$	$\eta^{(m)}$	$L^{(m)}$	$\theta_*^{(m)}$
Material (1)	1|2	5|15	3	−1
Material (2)	2|1	6|15	5	0
Material (3)	1|5	4|15	1	2

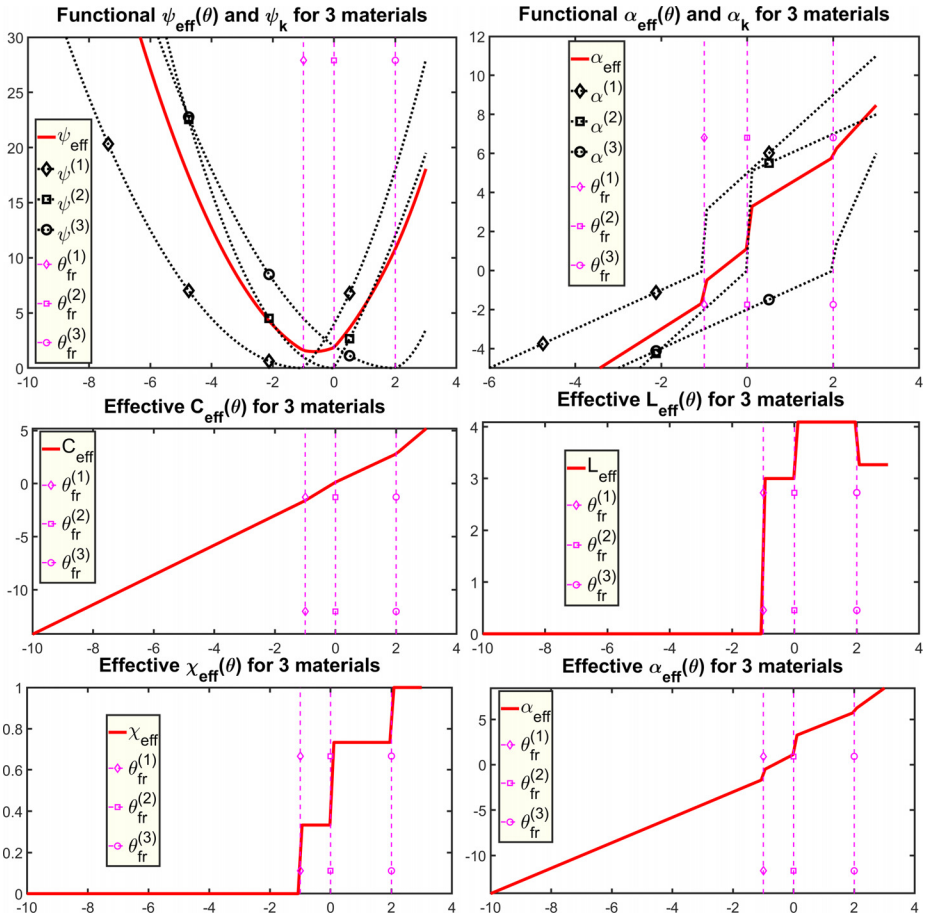

FIG. 3. *Illustration for Example* 3.1. *Plots of* $\psi_{eff}(\theta)$, $\alpha_{eff}(\theta)$, *and how they are built from* $\psi^{(m)}$, $\alpha^{(m)}$ *(top). Middle and bottom:* $\mathcal{C}_{eff}(\theta), \mathcal{L}_{eff}(\theta)$, *and* $\chi_{eff}(\theta)$, *as building blocks of* α_{eff} *following STEP* 2–5 *of Corollary* 3.2. *We indicate the freezing temperatures at which the properties have jumps.*

Next, we discuss upscaling conductivities to k_{eff}. Here we also connect our upscaling efforts to realistic data from porous media.

4.1. Results: Upscaling α for the basic and extended models. In section 4.1.1 we first upscale Model-ω-basic with $N_{MAT} = 2$ for rock and bulk water. In section 4.1.2 we upscale Model-ω-extended which accounts for Gibbs–Thomson effects in a collection of N_{MAT}-1 > 1 subdomains corresponding to the pores of a variety of characteristic sizes.

4.1.1. Upscaling α in Model-ω-basic to Model-Ω-basic. We now apply the discussion in section 3.2 to upscale $(\alpha_m^{(m)})$ for the rock-water mixture with $N_{MAT} = 2$ and $m = r, w$ described in section 2.2.2. The properties of $\Omega^{(w)}$ are identical to bulk water. For $\Omega^{(r)}$, we set $\theta_*^{(r)} = 0$ with $L^{(r)} = 0$ to simplify the notation and calculations.

We follow similar physical reasoning as in Example 3.1 to calculate the amount ηL of heat necessary to melt all the ice in $\omega_i^{(w)}$ in the pore domain ω when the temperature goes from far below to above freezing.

We next follow the steps in Corollary 3.2. We number the water material w as $m=1$, with $\theta_*^{(1)}=0$. The rock material is $m=2$, with $\theta_*^{(2)}=0$ but $L^{(2)}=0$. We recall porosity $\eta=\eta^{(w)}=\eta^{(1)}$ and $1-\eta=\eta^{(r)}=\eta^{(2)}$. Consistent with (3.11e) we get $\chi_{eff}(\theta)=(\eta^{(1)}+\eta^{(2)})\mathcal{H}(\theta)=\mathcal{H}(\theta)$, thus for this example $\chi_{eff}(\theta)=\chi_l^{(w)}(\theta)$ features only one jump at $\theta=0$. In turn, from (3.11f) for $\theta\geq 0$, $\mathcal{L}_{eff}(\theta)=\eta^{(1)}L+\eta^{(2)}0=\eta^{(w)}L^{(w)}=\eta L$ vanishes for $\theta<0$, and features only one jump at $\theta=0$. Next, the slopes c_{eff} of the regular part $\mathcal{C}_{eff}(\theta)=c_u\theta\chi_{eff}(\theta)+c_f\theta(1-\chi_{eff}(\theta))$ with (3.11c) are given by $c_{eff}|_{\theta<0}=\eta c_i+(1-\eta)c_r=c_f$ and $c_{eff}|_{\theta>0}=\eta c_l+(1-\eta)c_l=c_u$ as in (2.13),

$$\alpha_{eff}(\theta)=\mathcal{C}_{eff}(\theta)+L\eta\chi_{eff}(\theta);\ \ \chi_{eff}(\theta)=\mathcal{H}(\theta-\theta_*). \tag{4.1}$$

This gives α_{eff} as part of Model-Ω-basic. We note that in applications literature, e.g., [40, 39, 77] c_f and c_u are called "frozen" and "unfrozen" properties consistent with (2.6a).

Example 4.1 (upscaling model-ω-basic). We consider $\omega=(0,1)$[cm], with rock grains $\omega^{(r)}=(0,0.20)\cup(0.60,1)$, and water $\omega^{(w)}=(0.20,0.60)$. Now $\eta=0.40$, and we use thermal parameters from Table 5. We calculate and plot χ_{eff},α_{eff} for Model-Ω-basic, and compare to a selected χ^P,α^P in Model-Ω-empirical; see Figure 4. For illustration, we include plots of $\chi^{(w)},\alpha^{(w)}$ in Model-ω-basic.

Remark 4.1. We compare Model-Ω-basic to Model-Ω-empirical. We see that $\chi_{eff}(\theta)=\mathcal{H}(\theta-\theta_*)$ features exactly one jump at $\theta_*=0$, as a special case of what Example 3.1 illustrated. In consequence, we see that χ_{eff} is qualitatively different from any of the empirical SFC $\chi_l^P(\theta)$ in Model-Ω-empirical from section 2.3 which feature long tailed smooth behavior and have steep gradients only for very coarse-grained soils [40]. For fine-grained soils such as clay, χ_l^P is smooth and entirely dissimilar from χ_{eff} given in (4.1). These differences carry over to that of α^P and α_{eff}.

Now we see that upscaling Model-ω-basic and treating pore water as bulk water fails to give an effective model resembling any Model-Ω-empirical. The primary reason

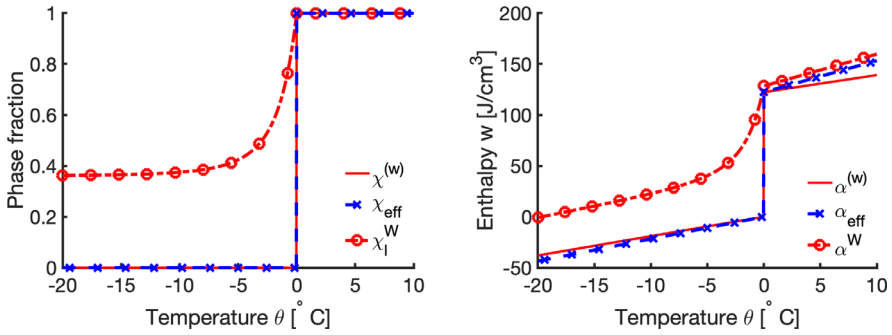

FIG. 4. *Illustration for Example* 4.1. *Shown is a comparison of the constitutive properties: liquid phase fraction (left) and enthalpy (right) between Model-ω-basic, Model-Ω-basic and Model-Ω-empirical. We plot $\chi^{(w)}(\theta)$ for Stefan problem in bulk water in Model-ω-basic in upscaled heterogeneous Stefan problem $\chi_{eff}(\theta)$ for rock-water in Model-Ω-basic, and the Darcy scale empirical model $\chi_l^W(\theta)$ in Model-Ω-empirical, same as that plotted in Figure* 2. *On the right we show the corresponding enthalpy graphs $w\in\alpha^{(w)}(\theta)$, $w\in\alpha_{eff}(\theta)$, and $w=\alpha^P(\theta)$. We emphasize the jumps of χ_{eff} and α_{eff} at $\theta=\theta_*=0$ in Model-Ω-basic which is absent in the empirical χ_l^P,α^P in Model-Ω-empirical.*

is that we have not accounted for the microphysics described in section 2.2.3. This is addressed in the next section.

4.1.2. Result: Upscaling α in Model-ω-extended to Model-Ω-extended. We now aim to improve the agreement with Model-Ω-empirical of concern in Remark 4.1. We incorporate the micro-physics of freezing in porous media from section 2.2.3, and in particular, we propose accounting for the depression of freezing temperatures in small pores.

To this end we modify our ϵ-model. We postulate that every REV $\omega(x)$ includes a collection of pores with a large variation of pore sizes. This feature is true in realistic porous media; see [21, 29, 14]; in particular, [14] reports for limestone that the largest pores make about 10% with diameters around 100 [μm], but the remaining pores have sizes below 10 [μm]. In turn, clay frequently features macro-, meso-, and micropores, with median pore sizes ranging from 100 through 1 through 0.01 [μm], respectively [21, 29]. See illustration in Figure 1, right.

Formally, we postulate that the water portion $\omega^{(w)}$ of an REV ω is made of several subdomains $\omega^{(w,m)}$, $1 \le m \le N_{WMAT}$, as well as of the rock material $r = N_{MAT} = N_{WMAT} + 1$. The subdomains $\omega^{(w,m)}$ correspond to some assumed volume fractions $(\eta^{(w,m)})_m$ and we have $\eta^{(r)} = 1 - \eta = 1 - \sum_{m=1}^{N_{WMAT}} \eta^{(w,m)}$. Next, we need the thermal parameters $c_l^{(m)}, c_i^{(m)}, L^{(m)}, k_l^{(m)}, k_i^{(m)}$ for each material in $\omega^{(w,m)}$. These can be distinct for each m but for simplicity we set these equal to those for the bulk water from Table 5. We distinguish each "material" (w,m) by its specific $\theta_*^{(m)}$ calculated with Gibbs–Thompson relationship (2.11) based on an assumed characteristic pore size $R^{(m)}$, ideally with $F^{GT} = F_0^{GT}$ for water as in Remark 2.1. We denote this collection $\mathcal{R} = (R^{(m)})_m$ and see that (2.11) gives a 1-1 map to the freezing temperatures in $\mathcal{T}$. We can now apply Corollary 3.2 to calculate χ_{eff} with (3.11e) for the given $\mathcal{D} = (\mathcal{R}, \mathcal{T})$. We also get α_{eff} incorporating the remaining data, each with N_{WMAT} jumps.

With this process we get the Model-Ω-extended with χ_{eff} resembling χ_l^P from Model-Ω-empirical. Since $\chi_{eff}(\theta)$ is a multivalued graph unlike the smooth function χ_l^P, we also fit χ_{eff} to some parametric model $\widetilde{\chi_{eff}^{model}}$ as part of some Model-Ω-extended-fit. Without fitting to a smooth curve, the upscaled model with multiple jumps requires substantial additional effort in implementation [74]. In addition, it raises the question on how α_{eff} compares to α^P from the empirical observations. These two statements motivate the idea of fitting. As for the choice of parametric models, one could use a variety of parametric models going beyond those used in geophysics literature. We aim, however, to address the connection to the empirical models of particular form. In the end, one can interpret the homogenization process which derives χ_{eff}, as an emulator of a physical experiment in which a discrete collection of experimental data points $(\theta_b, \chi_b)_b$ is collected, followed by fitting to some smooth parametric model $\widetilde{\chi_{eff}^{model}}$.

Beside qualitative agreement, a good test of our conceptual process is whether $\widetilde{\chi_{eff}^{model}}$ is reasonably close to some χ_l^{model} reported in the literature. We provide examples to address this question, assuming first that we know the distribution of pore sizes $\mathcal{R}$. Considering $\mathcal{R}$ as data creates a bit of a conundrum since these should be simultaneously compatible with the actual REV size $|\omega|$, and since we aim for the freezing point depression to be significant enough to be noticed in computations and in physical experiments.

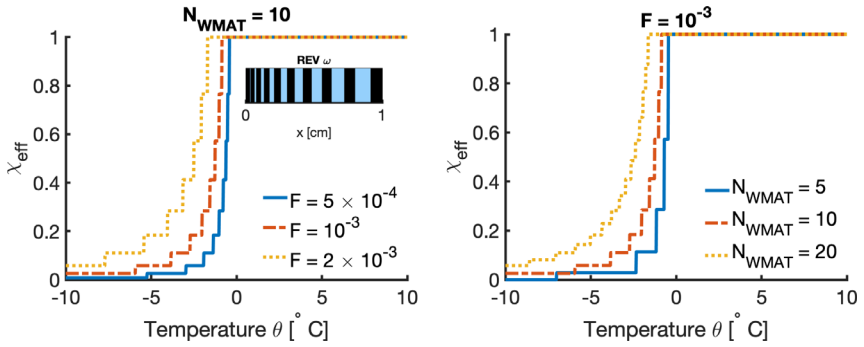

FIG. 5. *Illustration for Example* 4.2*: the dependence of the upscaled phase fraction* χ_{eff} *on the Gibbs–Thomson parameter* $F = F^{GT}$ *in* (2.11) *(left) and on the number of materials* N_{MAT} *(right).*

Example 4.2 (upscaling to model-ω-extended and fitting to model-Ω-extended-fit). We consider the REV $\omega = (0,1)$[cm] illustrated in Figure 5, with porosity $\eta = 0.5$. We consider $N_{MAT} > 2$ with the arrangement of phases as follows: the pore sizes $R^{(m)}$ were generated recursively using $R^{(m+1)} = R^{(m)} + U^{(m)}$, and $(U^{(m)})_{m=1}^{N_{MAT}-2}$ was generated uniformly from $[0.2, 1]$. The values $R^{(m)}$ were scaled next so that $\sum_m R^{(m)} = \eta|\omega|$. Next, we use (2.11) to compute the depression in the freezing temperature corresponding to an assumed pore size for which we heuristically set $R^{(m)} = \eta^{(w,m)}|\omega|$. To accommodate these, we use ad-hoc values $F^{GT} \in \{5\times10^{-4}, 10^{-3}, 2\times10^{-3}\}$. For each choice of N_{MAT} and F^{GT} we calculated the upscaled liquid fraction $\chi_{eff}(\theta)$ which we fit to some $\widetilde{\chi_{eff}^{model}}$. The results are plotted in Figure 5 and are given in Table 8.

We make the following observations. Already with $N_{WMAT} = 10$, the step functions χ_{eff} plotted approximate well some of the smooth relationships χ_l^P in Figure 2, with a large tail and freezing point depression of order 10[°C]. Second, as expected, increasing F^{GT} or N_{WMAT} increases the magnitude of the freezing point depression and decreases the maximum slope of χ_{eff}. Third, the parameter fit reported in Table 8 is, in general, agreement with the parameter range from literature, and is best for models W and M, and would improve, e.g., with larger N_{WMAT}.

Now we address the choice of F^{GT} in Example 4.2. In principle, we should consider only the physical value $F^{GT} = F_0^{GT}$ from Remark 2.1. However, as indicated there, the drop of θ_* by more than $10°C$ observed in nature requires very small radius R of a pore. Simultaneously, the smoothness of experimentally measured χ_l^P indicates that there is a wide range of pore sizes in permafrost soils, likely reaching from 10^{-9} to 10^{-4}[m]. We can include these submicron size pores along with larger pores in the model construction. However, an image or grid resolution for these would be at least 10^6 in one dimension which prevents us from the use of either imaging data, or of synthetically constructed computational domains. Therefore, without this high resolution, a good fit in Example 4.2 with an assumed $\mathcal{R}$ requires $F^{GT} >> F_0^{GT}$. Alternatively, one should fix the freezing temperatures $\mathcal{T}$ rather than the radii $\mathcal{R}$. This issue is relevant for validation as well as for the impending comparison between the pore- and the Darcy scale simulations in section 5.4.

Remark 4.2. If we are to interpret quite literally the decomposition of $\omega^{(w)}$ to subdomains $\omega^{(w,m)}$ in which one solves the pore-scale problem numerically, then $O(R^{(m)}) = \bar{R} \approx |\omega^{(w,m)}|$ as in Example 4.2. For this, we must accept an estimate for the order of magnitude $\bar{R} \approx O(10^{-2}|\omega|)$ corresponding to, e.g., $N_{WMAT} = 50$,

$\eta = 0.5$, to allow a reasonable discretization each with 10 cells per each $\omega^{(w,m)}$ for the total of about $O(10^3)$ grid cells in each ω. In other words, $R^{(m)}$ or $\bar{R}$ should not be too small. At the same time, from Remark 2.1 the physical choice of $F_0^{GT} = 10^{-7}$ corresponds to $\Delta\theta_* \approx 1°C$ only for small $R_0 = 10^{-7}$ [m], but to achieve a close fit of χ_{eff} to empirical χ_l^P from plots in Figure 2, we must have at least $|\theta_*^{(m)}| > O(1°C)$. Therefore, in this literally understood scenario when the physical size of REV and of $\mathcal{R}$ are matched, we conclude that a close fit between χ_l^P and χ_{eff} is obtained either when χ_{eff} is based only on $\mathcal{T}$, or if the process connecting $\mathcal{T}$ to $\mathcal{R}$ and the assumed $\omega^{(w,m)}$ follows with a scaled $F^{GT} = F_0^{GT}\frac{\bar{R}}{R_0} = 10^{-2}|\omega|$ or larger, as in Example 4.2. Another option is to consider REV ω which is physically much smaller, which contradicts the above statement about $\bar{R}$.

We demonstrate the scaling and fitting issues further in the next examples.

Example 4.3 (dependence of model-Ω-extended on N_{MAT} and the factor F^{GT}). We consider (a) $\omega = (0, 10^{-3})$ [cm] with $\eta = 0.50$ and $N_{MAT} = 51$ materials. In (b), we consider $\omega = (0, 1)$ [cm], and $N_{MAT} = 11$; the configuration of materials within the REV is shown in Figure 6. For both cases we generate $(R^{(m)})_m$ from a normal distribution $\sim N(0.1, 4 \times 10^{-4})$, and next scale so that $\sum_m R^{(m)} = \eta|\omega|$. We calculate $\theta_*^{(m)}$ from (2.11) with (a) $F^{GT} = F_0^{GT}$, and (b) with $F^{GT} = 10^{-3}$. We calculate the upscaled χ_{eff}, and we fit to $\widetilde{\chi_{eff}^{model}}$; these are shown in Figure 6, with data in Table 9.

We see that the fitting parameters for $\widetilde{\chi_{eff}^{model}}(\theta)$ are within the range reported in the literature. The example illustrates well the connection between the fitted models and Model-ω-extended.

The examples have shown the success of our conceptual construction of Model-ω-extended in achieving close agreement with Model-Ω-extended after upscaling.

4.1.3. Validation of α_{eff} in Model-Ω-extended. A meaningful validation study would require a comprehensive dataset for some soil including a pore size distribution $\mathcal{R}$ (or of freezing temperatures $\mathcal{T}$), soil-specific SFC χ_l^P, and the knowledge of porosity η. Such comprehensive data is not available at this time, but we attempt

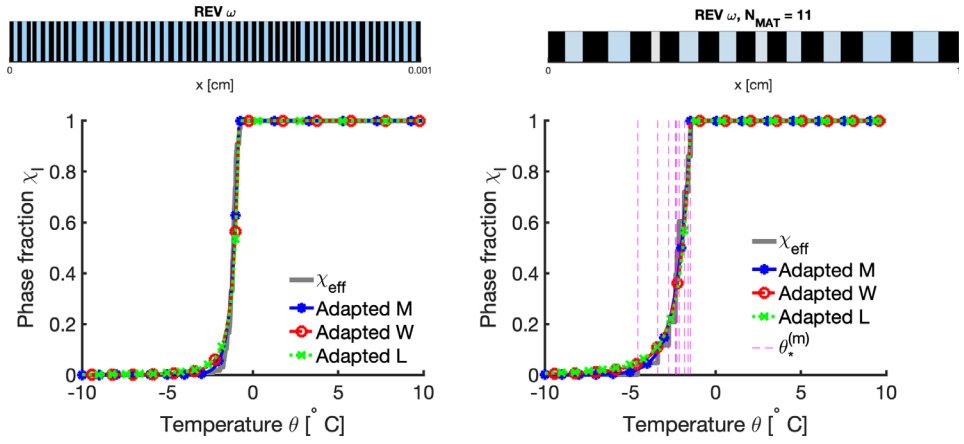

FIG. 6. *Results of Example* 4.3*: plot of upscaled phase fraction* $\chi_{eff}(\theta)$ *and of fitted models* $\widetilde{\chi_{eff}^{model}}(\theta)$ *for model* $= L, W, M$*. Left: case* (a) *with* $F^{GT} = F_0^{GT}$*. Right: case* (b) *with* $F^{GT} = 10^{-3}$*. Domain sizes and REVs are shown on top.*

realistic setting using only data on $\mathcal{R} = (R^{(m)})_m$ and the associated volume fraction $(\eta^{(w,m)})_m$ from applications literature; we refer to [21, 29] as a resource. We also use X-ray micro-CT images [48, 49, 70, 50, 59], even if these do not resolve well the tiniest pores.

We start with some empirical $\chi_l^P(\theta)$ and η. Next, we find the step function $\chi_{eff} = \Pi_{\mathcal{T}}(\chi_l^P)$ as the L^2 projection of χ_l^P on some assumed grid $\mathcal{T}$. Clearly, the choice of $\mathcal{T}$ determines the quality of the process and of the fit of $\chi_l^P \approx \chi_{eff}$. Since χ_l^P features steep gradients close to $\theta_* = 0$, $\mathcal{T}$ is usually graded with more points towards $\theta_* = 0$. We also have the pore sizes $\mathcal{R} = (R^{(m)})_m$ from (2.11) assuming some F^{GT}.

Next, we extract the volume fraction $\eta^{(w,m)}$ of each material (w,m) from (3.11e) as the jump $\eta^{(w,m)} = [\chi_{eff}]|_{\theta_*^{(m)}}$ of the step function χ_{eff} at each of the $\theta_*^{(m)}$, $1 \le m \le N_{WMAT}$. For $\theta_*^{N_{WMAT}}$ we have $\eta^{w,N_{WMAT}} + 1 - \eta = [\chi_{eff}]|_{\theta_*^{(N_{WMAT})}}$ so that $\eta^{(r)} = 1 - \sum_m \eta^{(w,m)}$.

We can next compare literature data as in the next example.

Example 4.4 (validation of Model-Ω-extended with pore size distribution data). We start with the SFC given by χ_l^M with parameters $\chi_{res}^M = 0, b^M = 0.2, \theta_*^M = 0$, porosity of $\eta = 0.5$, and $F^{GT} = F_0^{GT}$; see Figure 7 for illustration. For expository purposes, we start with $N_{WMAT} = 5$; see Table 4 for $\theta_*^{(m)}$, the calculated characteristic pore size $R^{(m)}$ and volume fractions $\eta^{(w,m)}$. We consider next large $N_{WMAT} = 50$ and obtain a better fit of χ_{eff}; we plot the histogram of $(R^{(m)}, \eta^{(m)})_m$ in Figure 7, with a comparison to the pore size distribution in [59, Figure 6] for silty loam.

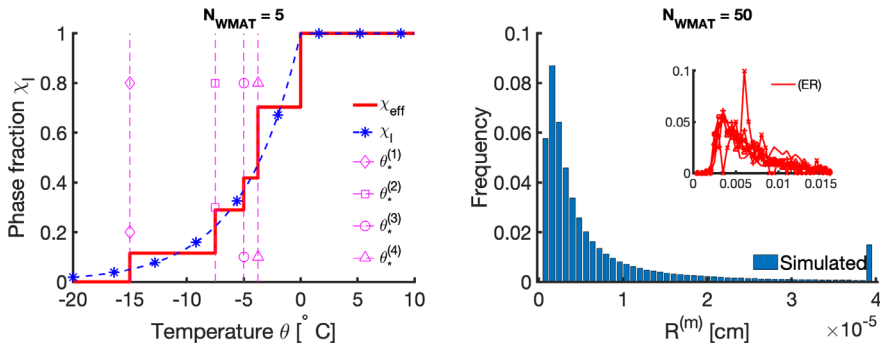

FIG. 7. *Illustration of Example* 4.4*: approximating a given SFC curve* χ_l^P *by some step function* χ_{eff} *based on a set of* $N_{WMAT} = 5$ *points* $\theta_*^{(m)}$*. Left: approximation of* $\chi_l^M \approx \chi_{eff}$ *when* $N_{WMAT} = 5$*. Right: with* $N_{WMAT} = 50$ *we have a better fit of* $\chi_l^P \approx \chi_{eff}$ *with more points in* $\mathcal{T} = (\theta_*^{(m)})_m$*; we show the histogram of pore size distribution* $R^{(m)}$ *compared to that from* [59]*, annotated as (ER) in the legend (inset, same units of radii).*

TABLE 4

Results of Example 4.4 *with* N_{WMAT}=5*: the pore radii and volume fractions for the SFC plotted in Figure* 7*.*

Parameter	Material (m)					
	(1)	(2)	(3)	(4)	(5)	(6)
$\theta_*^{(m)}$ [°C]	-15	-7.5	-5	-3.75	0	0
$R^{(m)}$ [cm]	8.000×10^{-7}	1.600×10^{-6}	2.400×10^{-6}	3.200×10^{-6}	–	–
$\eta^{(m)}$ [–]	5.778×10^{-2}	8.696×10^{-2}	6.422×10^{-2}	1.427×10^{-1}	1.482×10^{-1}	5.000×10^{-1}

As shown in Figure 7 we have good qualitative agreement with [59, Figure 6], but there is a scaling discrepancy of roughly 100 between pore radii we find and those reported in literature. We already addressed the scaling issue in Remark 4.2 and note that the data in [59, Figure 6] uses very small range of $\mathcal{R}$. Here we would have $|\omega| \sim O(10)$ [μm].

Next, we attempt the validation process in the opposite direction. From a given histogram of $\mathcal{R}$, we extract the volume fractions $\eta^{(w,m)}$, and for each $R^{(m)}$ we calculate $\mathcal{T} = (\theta_*^{(m)})_m$. The homogenization process in (3.11e) gives $\chi_{eff}(\theta)$ which we can fit to a selected parametric model $\widetilde{\chi_{eff}^{model}}(\theta)$.

Example 4.5 (cross-checking of Model-Ω-extended with inverse modeling). We consider (a) one of the pore size distributions from [59] for a small sample of silty loam. We also consider (b) the pore size distribution of Berea sandstone in [29], normally distributed with mean $\mu = 0.002$ [cm] and an estimated standard deviation $\sigma = 0.001$ [cm] to replicate the behavior reported in [29, Figures 3–7]. For both examples, we assume $\eta = 0.5$. We use $F^{GT} = F_0^{GT}$, and derive Model-Ω-extended with $\chi_{eff}(\theta)$ fitted to $\widetilde{\chi_{eff}^{model}}(\theta)$ for each $model = M, W, L$ shown in Figure 8, and with parameters in Table 9.

In (a) the range of pore sizes is relatively small of 10–150 [μm], thus the corresponding range of freezing temperatures is small at most 0.01 [°C], resulting in a steep profile of χ_{eff} and a poor fit of the models $\widetilde{\chi_{eff}^{model}}$ which feature steeper gradients than those plotted in Figure 2. The distribution in (b) gives a better fit, but the freezing depression is likely underestimated to be only of 0.1 [°C].

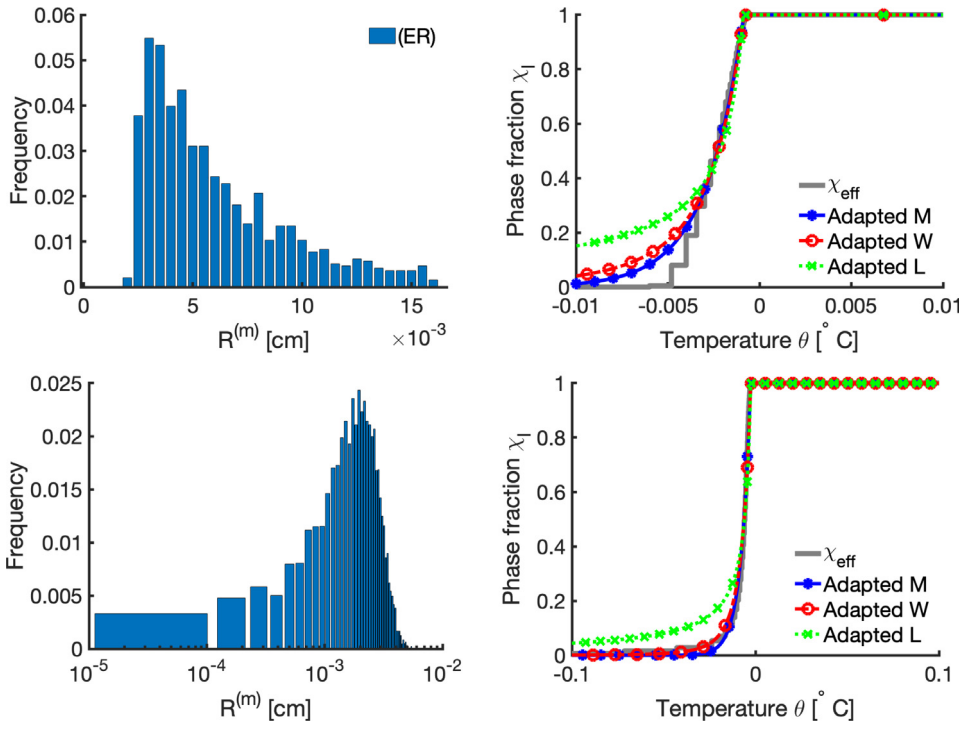

FIG. 8. *Illustration for Example* 4.5*: constructing* $\chi_{eff}(\theta)$ *and* $\widetilde{\chi_{eff}^{model}}(\theta)$ *for the given pore size distribution from* [59] *annotated as (ER) in the legend (top) and for Berea sandstone from* [29].

In the end we believe that the examples we provide show success of the proof-of-concept construction of upscaling Model-ω-extended to Model-Ω-extended.

4.2. Results: Upscaling heat conductivity $(k^{(m)})_m$ from Model-ω to $k_{eff}(\theta)$ in Model-Ω. Here we work to derive effective conductivity k_{eff} and some of its approximations $\widetilde{k_{eff}}$ which we compare to the simple averages k^A, k^G, k^H given by (2.15). Since we do not have physical data for conductivities in small pores, we use the properties for bulk water, thus there is no difference in calculating k_{eff} from Model-ω-basic and Model-ω-extended. The main challenge we describe and address is a significant nonlinear dependence of the upscaled conductivities on the actual phase distribution rather than only on the volume fractions of ice within $\omega^{(w)}$. This dependence calls for construction of a reduced model.

Heat conductivity for composites is an important topic both for practical studies of unsaturated as well as ice- or hydrate-filled soils [68, 9, 11], and from the theoretical point of view [36]. In particular, of interest are both the homogenized conductivity tensors as well as the upper and lower bounds such as k^A and k^H on their eigenvalues, respectively. Composites with nonzero thermal contact resistance are also important [60, 31] but are outside our scope. Tighter bounds can be obtained with Hashin–Shtrikman formulas when $N_{MAT} = 2$; see [36, secs. 2.6–2.7], but are not easily computable for rock and water in two phases.

4.2.1. Theoretical set-up. To calculate k_{eff}, we require $(k_p^{(m)})_{m=1}^{N_{MAT}}$ for each material m and phase $p = l, i$. For $m = r$ we set $k^{(r)} = k|_{\omega^{(r)}} = k_r$, and assume $\omega^{(r)}$ is known. For $k|_{\omega^{(w)}}$ as in Assumption 2.1 we only consider phase dependence, i.e., we choose from k_l, k_i. We also set $k|_{\omega_l^{(w,m)}} = k_l, k|_{\omega_i^{(w,m)}} = k_i$ in each $m = 1, N_{WMAT}$ regardless of the pore size in $\omega^{(w,m)}$; the more general case would require the knowledge of the heat conductivity of the undercooled water and/or small pores for which we lack sufficient literature at this time.

Given some $\bar{\theta}(x) = \theta_0$, the effective heat conductivity $k_{eff}(\theta_0) \in \mathbb{R}^{d\times d}$ for the heterogeneous Stefan problem (2.8) is given by (3.4) as part of Proposition 3.1. To solve (3.4b) for $(\xi_j)_{j=1}^d$, we need to know the geometry of the materials and phases $\omega_l^{(w)}, \omega_i^{(w)} \subset \omega(x)$ corresponding to θ_0.

Remark 4.3. In d=1, $k_{eff}(\theta_0)$ equals exactly k^H which only depends on the volume fraction of the materials rather than their geometry, which can be approximated from the known $\chi_{eff}(\theta_0)$.

We can also consider some approximations $\widetilde{k_{eff}}$ discussed in section 3.3. In addition, we consider reduced models defined next.

4.2.2. Proposed practical reduced model for $k_{eff}(\theta)$. For $d > 1$, the distribution of $\omega_l^{(w)}$ corresponding to θ_0 is not unique. In fact, for a given θ_0, there are infinitely many possible different realizations $(\theta(y)_a)_a, y \in \omega$: $\langle \theta(\cdot)_a \rangle = \theta_0$, with the corresponding geometry $(\omega_l^{(w)})_a$; each yields a different $(k_{eff})_a$. The second challenge is that the dependence on θ_0 is implicit.

To make the calculations of $k_{eff}(\theta)$ useful for coarse-scale computational models, we propose a reduced model, a comprehensive look-up library for each fixed rock–water domain $\omega^{(r)}$. A desired value of $k_{eff}(\theta)$ is given by an interpolation of the precalculated values $(k_{eff}(\theta_b))_b$ drawn from a probability distribution of $(\theta_b)_b$, as is common in reduced order models [52].

Remark 4.4. The parametrizations of probability distributions $(k_{eff}(\theta_b))_b$ can be calculated offline: for each θ_b and a given $\omega^{(r)}$ we build a desired number N_a of

"realizations" of $(\omega_l^{(w)})_a$ with one of the following data–based or simulation strategies: (i) postprocessing the pore-scale images [14, 59], or (ii) simulations of $(\theta(y,t))_a$ corresponding to some initial data and energy input scenarios for which the time snapshots of averages equal θ_b. Alternatively, one can pursue (iii) via stochastic or statistical mechanics simulations of plausible phase configurations compatible with the microphysics; see [50].

A different reduced model strategy is possible for pore modifications due, e.g., to biofilm growth around the grains such as in the work [7].

4.2.3. Results on k_{eff}. We illustrate now the idea in section 4.2.2, and compare k_{eff} to the approaches in permafrost literature which calculate $k^P = k^P(\theta_0)$ as one of k^A, k^G, k^H given by (2.15); these do not distinguish the different geometries $(\omega_l^{(w)})_a$. In Example 4.6 we follow up on point (i) from Remark 4.4, and assume $\omega^{(w,l)}, \omega^{(w,i)}$ are known from imaging. In Example 4.7 we assume as in (ii) that $\omega^{(w,l)}, \omega^{(w,i)}$ are known from simulations.

Example 4.6 (upscaling thermal conductivities with a phase arrangement from imaging). We consider pore geometries taken from [50, Figure 1A] with ω shown in Figure 9, with voxel resolution 535×536. We consider first cases (1)–(2) with $\omega^{(w)}$ in one phase only, and then cases (3)–(4) with $\omega^{(w)}$ partitioned into two phases. We assume material properties as in Table 5, and find the upscaled k_{eff}, its approximation $\widetilde{k_{eff}}$, and the simple averages given by (2.15). These values are reported in Table 6.

Now we discuss the results: the geometry of ω is close to "isotropic" without any particular layered or skew trends, even when multiple phases are present. Therefore, it is not a surprise that the tensor k_{eff} reflects this "isotropy": the diagonal values of k_{eff} are close to one another, and the off-diagonal values $k_{eff,12}, k_{eff,21}$ (not shown in Table 6) are of order 10^{-5}. Next, the values of $\widetilde{k_{eff}}$ are within less than 1% of k_{eff} even when additional eight digits are considered (not shown). Finally, in each case

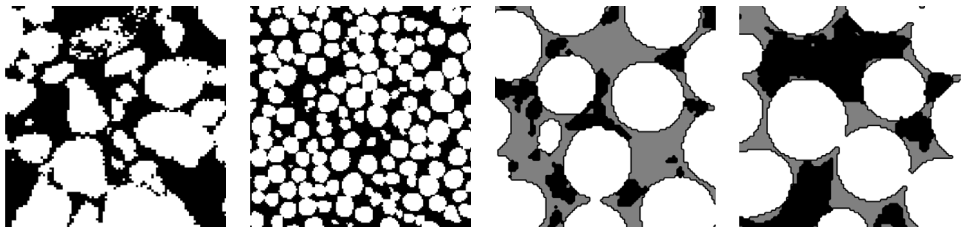

FIG. 9. *Pore-scale images of $\omega(x)$ from Example* 4.6. *Rock grains in white. In* (1)–(2) *water is in black. In* (3)–(4)*, water is in gray, and additional solid phase is in black. The effective k_{eff} and its approximations are given in Table* 6.

TABLE 5

Thermal properties of rock and water materials assuming water has properties of bulk water. (The grains are considered "frozen" for $\theta < 0$ and "unfrozen" for $\theta > 0$.) This convention is useful for algebraic formulas employed in section 4.1.1.

Material	$c_i^{(m)} \mid c_l^{(m)}$	$k_i^{(m)} \mid k_l^{(m)}$	$L^{(m)}$	$\theta_*{}^{(m)}$	Reference
Unit	[J/m^3°C]	[J/m s°C]	[J/m^3]	[°C]	
Material (w)	$1.90 \times 10^6 \mid 4.19 \times 10^6$	$2.30 \mid 0.58$	3.06×10^8	0	[58]
Material (r)	$2.36 \times 10^6 \mid 2.36 \times 10^6$	$1.95 \mid 1.95$	0	0	c_i, k_i: [78]

TABLE 6
Upscaled values k_{eff} of heat conductivity k from Example 4.6 corresponding to the geometries shown in Figure 9, and its approximations $\widetilde{k_{eff}}$ as well as k^A, k^G, k^H.

Case	η	$\eta^{(w)_i}$	χ_i	k^A	k^G	k^H	$k_{eff,11}$, $k_{eff,22}$	$\widetilde{k_{eff,11}}\widetilde{k_{eff,22}}$
(1)	0.4413	0	0	0.01345	0.01142	0.00955	0.01149 0.01166	0.01149 0.01150
(2)	0.4395	0	0	0.01347	0.01144	0.00956	0.01168 0.01161	0.01168 0.01162
(3)	0.4099	0.3558	0.1499	0.0164	0.0146	0.0123	0.01492 0.01471	0.01492 0.01467
(4)	0.4136	0.2679	0.6478	0.01844	0.01708	0.01496	0.01717 0.01727	0.01721 0.01720

k^G is within less than 1% of the diagonal entries of k_{eff}, but k^A and k^H can be as much as 10–20% different from k^G. In the end, the values $k^G\mathbf{I}$ as well as $\widetilde{k_{eff}}$ appear to provide a very good approximation to upscaled conductivities k_{eff}.

Next we consider a layered phase arrangement, with the realizations of $(\omega_l^{(w)})_a$ obtained via a transient simulation of heat equation at the pore-scale for a scenario of thawing due to heat input from bottom boundary.

Example 4.7 (upscaling thermal conductivities with a phase arrangement given from simulations). We consider pore scale geometry shown in Figure 10, assume material properties in Table 5, and conduct simulations of thawing, following [5. Example 5.4.2]. For every time step t^n of the simulation, we have a different geometry of $(\omega_l^{(w)})_n$, with selected snapshots shown in Figure 10. We calculate the volume fraction $(\chi_l)_n = \langle \chi(\cdot, t^n)\rangle$, $\langle\theta\rangle^n$, and upscaled k_{eff} plotted in Figure 10; we omit the off-diagonal entries of k_{eff} which are about 10^{-5} smaller than the diagonal entries.

This example demonstrates a different pattern than in Example 4.6. While the manner of upscaling seems insignificant since $k_{eff} \approx \widetilde{k_{eff}}$, we see a drastic difference between k_{eff} and k^A, k^G, k^H. As shown in Figure 10, the thawing process follows by design from the bottom to the top of the domain $\omega(x)$. As a result, the arrangement of phases (materials) at each time step n resembles a layered medium with inclusions, with layers building up in the vertical x_2 direction. Unlike in Example 4.6 we see strong anisotropy with up to 50% difference between the horizontal and vertical components of the conductivity $k_{eff,11} \neq k_{eff,22}$ which, as expected, are close but not equal to the arithmetic and harmonic averages, respectively. This feature, typical for layered media, is somewhat moderated due to the presence of rock inclusions. Finally, the geometric average k^G remains within 20 to 25% of the upscaled values $k_{eff,11}$ and $k_{eff,22}$ and more or less splits their difference.

In the end we see significant difference between the upscaled heat conductivities k_{eff} found using different approaches. It is natural to wonder how this difference impacts the Darcy scale models. We follow up with a study of sensitivity to k^P in permafrost models in section 5.3; we also discuss the choice of k_{eff} in the comparison between the pore- and the Darcy scale to be reported in section 5.4.

5. Computational results. In this section we provide simulation results to illustrate the upscaling heterogeneous Stefan problem in Model-ω-extended (2.8) with data $(\alpha^{(m)}, k^{(m)})_m$ to the effective model Model-Ω-extended (3.2) with data (α_{eff}, k_{eff}) and their practical approximations $(\widetilde{\alpha_{eff}}, \widetilde{k_{eff}})$ in Model-Ω-extended-fit. These were defined in sections 4.1.2 and 4.2.

In section 5.1 we provide literature notes. In section 5.2 we outline our P0-P0 scheme. In section 5.3 we present a sensitivity study on k_{eff} and k^P at the Darcy scale. In section 5.4 we present our main result: a computational comparison of the pore-scale and the Darcy-scale models.

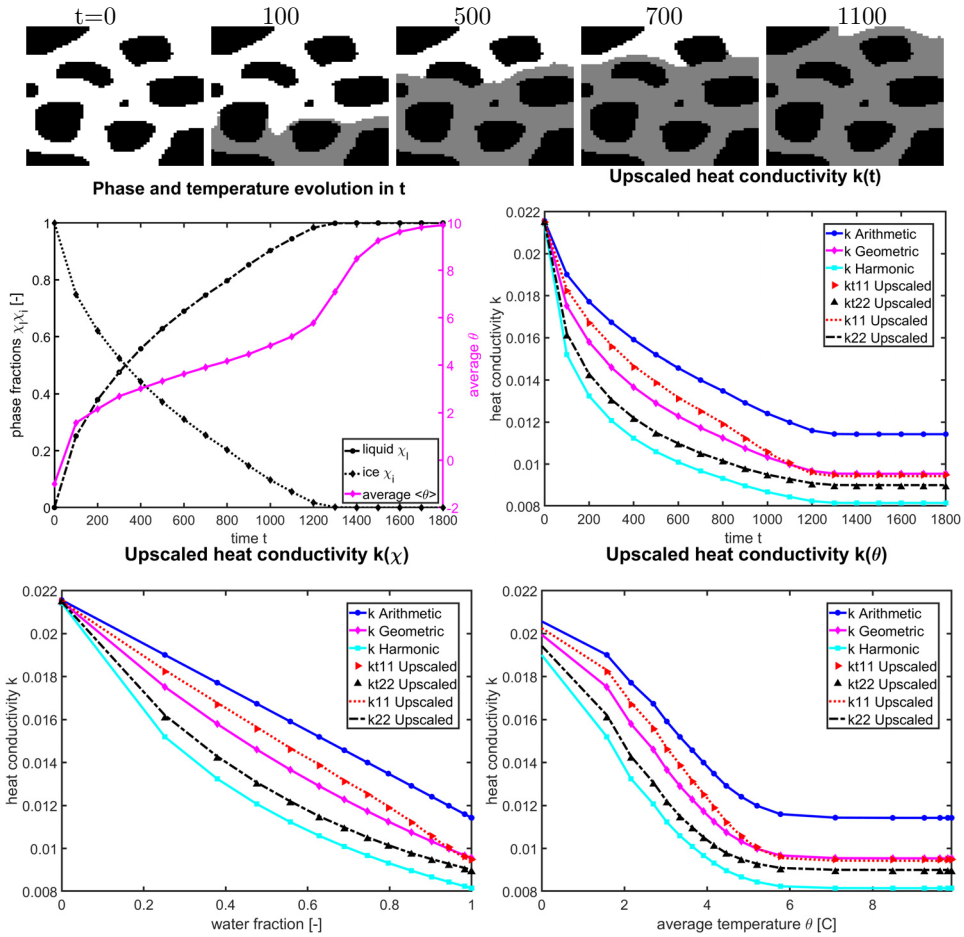

FIG. 10. *Illustration for Example* 4.7. *Top: evolution of the geometry* $\omega(x)$ *in time: grains* $\omega^{(r)}$ *black, ice* $\omega_i^{(w)}$ *in white, and liquid* $\omega_l^{(w)}$ *in gray. Middle and bottom: effective thermal properties corresponding to the evolving* $\omega^{(w,l)}$. *Middle: plots of average phase fractions* $\eta_l(t)$, $\chi_l(t)$, *and* $\chi_i(t)$, *and of upscaled* $k_{eff}(t)$, *approximated* $\widetilde{k_{eff}}(t)$ *and averaged values of heat conductivity. Bottom: plots of* $k_{eff}(\chi_l)$ *and* $k_{eff}(\langle\theta\rangle)$.

5.1. Literature notes on approximation of Stefan problem and nonlinear degenerate parabolic problems. We start by acknowledging the wealth of literature on the subject including the classical contributions on monolithic (no front-tracking) approaches to the homogeneous Stefan problem in [37, 58, 35, 41, 71, 25]. These, however, do not apply to the heterogeneous version in our Model-ω, and our recent review accompanying the schemes for heterogeneous Stefan problem in [6] includes an extensive discussion of the P1-P1 schemes [61], P1-P0 schemes involving the Chernoff formula [35, 41], and approximations using phase relaxation [71, 25].

As concerns the Darcy scale permafrost models similar to Model-Ω-empirical, we see from the plots in Figure 2 that $\alpha^P(\theta)$ features nonlinearity with a singular derivative at $\theta = \theta_*$ somewhat different than in the degenerate but smooth nonlinear parabolic equations considered, e.g., in [3, 63, 76, 51, 54, 53]. In particular, linear rates have been derived in [3, 63] which can be extended to quadratic rates under strict smoothness requirements [3].

Meanwhile, the applications literature has produced simulations of Model-Ω-empirical with focus on simulations rather than convergence analyses included, e.g., in [20, 75, 23, 40, 38].

We are not aware of any work that would fit the multivalued Model-Ω-extended with multiple jumps, but we are working on a manuscript on this topic [74].

5.2. Algorithm. We start by briefly outlining the approximation techniques for the heterogeneous Stefan problem (2.8) at the pore-scale, and for the permafrost model at the Darcy scale for (2.12). At both scales, we use rectangular (voxel) grids, and a fully implicit in time scheme, approximating θ and w each by piecewise constants (hence denoted by P0-P0), and fluxes with $RT_{[0]}$ finite elements. This P0-P0 approximation scheme is implemented as CCFD (cell-centered finite difference) scheme, also interpreted as a finite volume scheme. It is solved for the primary scalar unknowns

$$w^n + \tau A(\theta^n)\theta^n = w^{n-1} + \tau f^n;\ n > 1, \tag{5.1a}$$

where $w^n = (w_j^n)_j$, $\theta^n = (\theta_j^n)_j$ are the vectors of discrete approximations to w, θ at time t^n and at the cell centers x_j of some rectangular grid covering Ω. We have $w^0 = (w_{init}(x_j))_j$. Also, τ is the time step, A is a discrete "diffusion" nonlinear operator built from the phase dependent heat conductivities and which incorporates the Dirichlet boundary conditions, and f^n approximates the source term which includes Neumann boundary data, if relevant. The system is closed with a relationship

$$g_j(\theta_j^n, w_j^n) = 0 \text{ at every grid point } x_j. \tag{5.1b}$$

Here the relationship g_j expresses the model-specific pointwise connection between θ and w. In the heterogeneous Stefan problem, let $x_j \in \Omega^{(m)}$ for some m; we work with the function $g_j(\theta, w) = \theta - (\alpha^{(m)})^{-1}(w)$; the function $(\alpha^{(m)})^{-1}(w)$ is a continuous nondecreasing Lipschitz function differentiable everywhere except at $w = 0$ and $w = L^{(m)}$. In empirical Darcy-scale models we work with $g_j(\theta, w) = g(\theta, w) = w - \alpha^P(\theta)$; the function α^P strictly monotone, continuous, globally Lipschitz, and differentiable everywhere except at $\theta = 0$. The approach is robust for the pore-scale models (3.1) and approximations to $w^\epsilon, \theta^\epsilon$ and the Darcy-scale models (2.12) with approximations to w^P, θ^P; we show in [6, 74] that the scheme converges at the linear rates, at least for the $d = 1$ examples and in the norms we consider.

The nonlinear algebraic system (5.1) is solved with Newton iteration which generally requires that all nonlinear functions are at least Lipschitz with a Lipschitz inverse. This holds for the pore- and the Darcy-scale models with (5.1b) described above: the Newton iteration is well defined and reasonably robust as long as adaptive time-stepping is used.

However, when approximating (θ^{eff}, w^{eff}), the solutions of the effective model (3.2), we have $g(\theta, w) = w - \alpha_{eff}(\theta)$ given by (3.7), and the solver for (5.1b) presents new challenges since α_{eff} features a mixture of several jumps and jumps in slopes. We find that the Newton iteration has difficulty converging without additional algorithmic improvements; these deserve special attention deferred to another venue [74]. Therefore in this paper we use a smooth approximation $\widetilde{\alpha_{eff}}(\theta)$ to α_{eff} discussed in section 3.2, for which Newton iteration works similarly to that for the empirical models $\alpha^P(\theta)$. This means that in the end, we find the approximations $(\widetilde{\theta^{eff}}, \widetilde{w^{eff}})$ rather than (θ^{eff}, w^{eff}).

5.3. Sensitivity study. We now address the issue of the dependence of the simulations of the Darcy-scale model on the conductivity value, which we believe

is significant. We consider $\Omega = (0,10)$[cm], $\eta = 0.43$, and $\chi_l^P(\theta) = \chi_l^M(\theta)$, with $\chi_{res} = 0, \theta_* = 0$, and $b = 0.16$. We use $w_{init}(x) = const = \alpha_{eff}(\theta_0)$ with $\theta_0 = -7$[°C] representing a frozen state. We discretize with $M = 50$ and $\tau = 10$[s], and simulate $\theta(x,t), t \in (0,T]$ with $T = 10,000$[s] sufficient for about quarter of the sample to thaw due to the boundary conditions

$$\theta(0,t) = \theta_0, \quad \theta(10,t) = 5. \tag{5.2}$$

We conduct two simulations. First, we focus on the "value" of k_r which influences $k^P(\theta)$.

Example 5.1 (study of sensitivity of solutions to Model-Ω to the heat conductivity k_r). We approximate $\theta(x,t)$ using $k_r = 1.95$ from Table 5. We also find $\theta^{new}(y,t)$ corresponding to some k_r^{new} chosen to be within 20% difference from k_r, and drawn randomly from a uniform distribution from $[1.56, 2.34]$. The temperature and enthalpy profiles for $k^P = k^A$ calculated at each k_r^{new} are shown in Figure 11. We find that the simulated $|\theta^{new}(x,t) - \theta(x,t)|$ can be as much as $\approx 0.74°$, which represents about 6% of the range of simulated temperatures.

Second, we keep k_r fixed, and study the sensitivity to the choice of k^P.

Example 5.2 (study of sensitivity of solutions to Model-Ω to the choice of parametrization k^P). We simulate $\theta^A(x,t), \theta^G(x,t), \theta^H(x,t)$ with the same scenario as in Example 5.1 but choosing, respectively, $k^P(\theta)$ to be k^A, k^G, or k^H given in (2.15). The results shown in Figure 12 show a difference $\max_{x,t} |\theta^A(x,t) - \theta^H(x,t)| \approx 1.45$[°C] which is about 15% of the range.

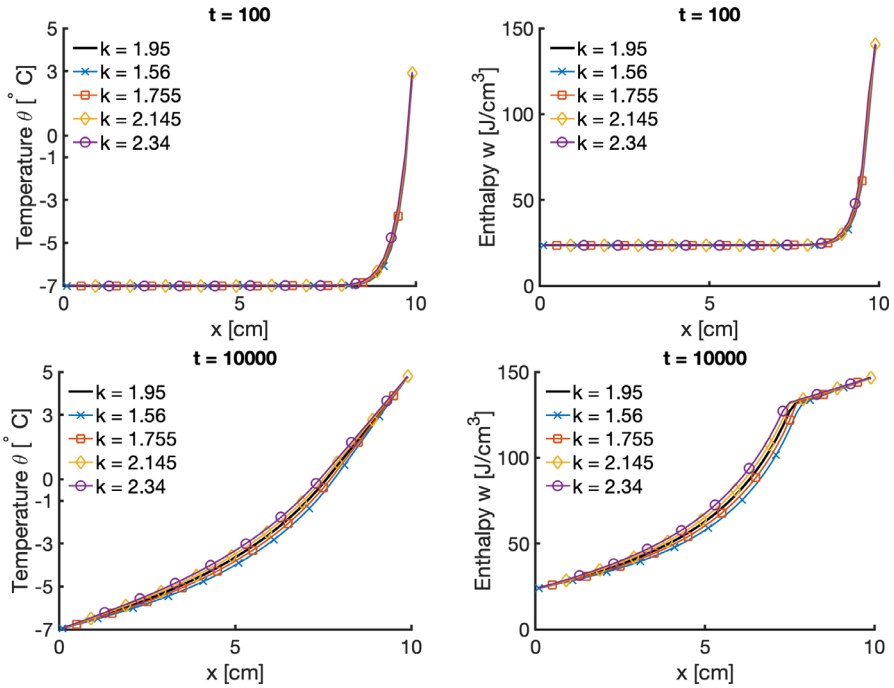

FIG. 11. *Temperature θ (left) and enthalpy w (right) profiles at $t = 100$ (top), and $t = 10,000$ [s] (bottom) for Example* 5.1. *The units in the legend for $k = k_r$ are* [J/m s°C].

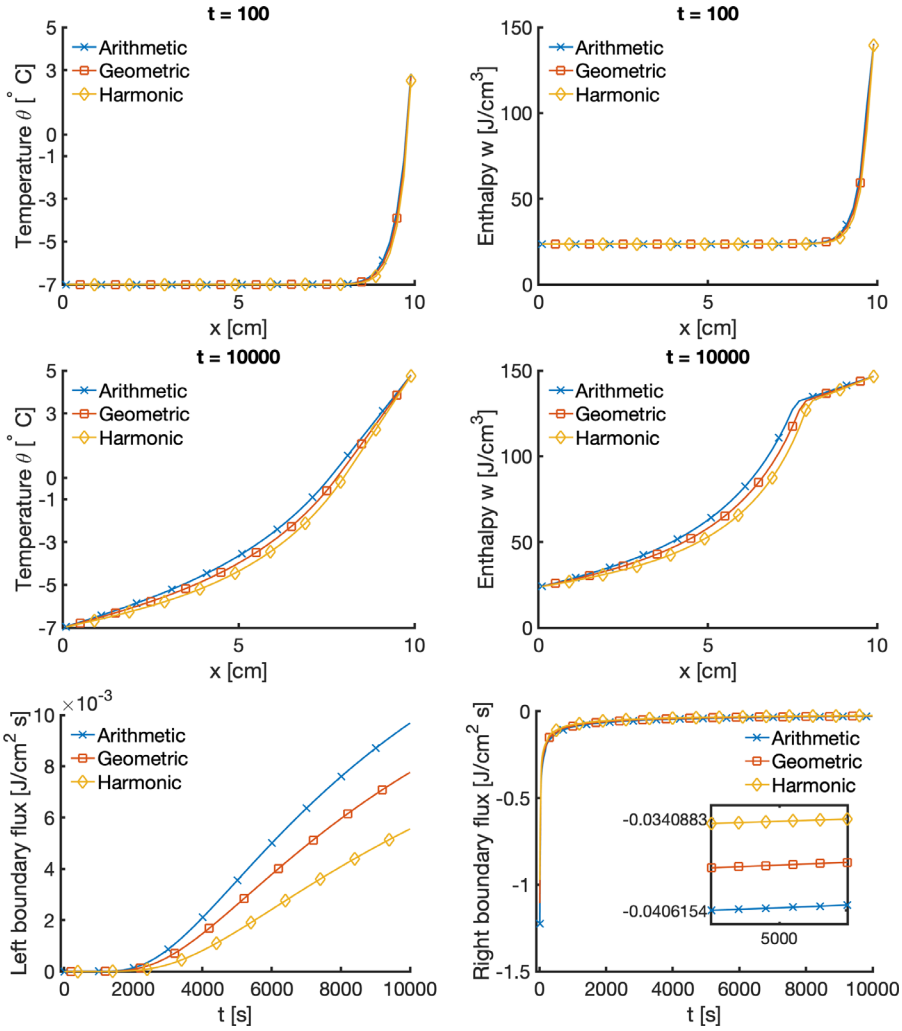

FIG. 12. *Temperature θ (left) and enthalpy w (right) at $t = 100$ (top) and $t = 10,000$ [s] (middle) for Example 5.2 comparing the use of k^A, k^G, and k^H. Also shown (bottom) are the normal boundary flux values over time.*

These two examples show substantial sensitivity of the solutions to the values and the choice of k^P. This fact plays a significant role in the quality of upscaling considered below.

5.4. Comparison between the pore-scale and the Darcy-scale models. In this section we illustrate the main result of this paper: we show that one can effectively upscale the heterogeneous Stefan problem with N_{REV} pores to the Darcy-scale permafrost model with data derived from upscaling the pore-scale data.

We work in $d = 1$ in which $\epsilon_0 = \frac{10}{N_{REV}}$ represents the actual size $|\omega|$ of the pore domain $\omega = (0, 1)$ [cm] relative to the size of $\Omega = (0, 10)$ [cm]. We choose the REV to be the same as in Example 4.3, with the pore geometry given in Figure 6, and porosity $\eta = 0.45$. Rock-fluid data is in Table 5.

The choice of $d = 1$ allows various simplifications; in particular, we recall that in one spatial dimension $k_{eff}(\theta)$ is known to be exactly equal k^H for a geometry $\omega_l^{(w)}$ corresponding to θ. This choice allows one us to focus on the features of the upscaling specific to the Stefan problem.

For initial and boundary conditions, we use the same scenario as in Examples 5.1 and 5.2 for the evolution from the initially frozen state towards a partial thaw due to the heat applied through Dirichlet condition on the right-hand side.

With the data as above, we approximate the solutions $(\theta^\epsilon, w^\epsilon)$ to the actual pore-scale model (2.8) implemented with the scheme (5.1). We also find the approximations to $(\widetilde{\theta^{eff}}, \widetilde{w^{eff}})$ to the Darcy-scale model (3.2), again with (5.1), and compare these to the pore-scale model solutions. When referring to these approximations, we suppress any notation for the spatial or temporal discretization.

For the Darcy-scale model, we build χ_{eff} as shown in Example 4.3(b), and calculate next $\widetilde{\alpha_{eff}(\theta)}$ built from the pore-scale model as described in section 3.2. Next, we construct $\widetilde{\alpha_{eff}^{model}}$ through a fit of χ_{eff} to one of the parametric models $\widetilde{\chi_{eff}^{model}}$, $model = L, W, M$ discussed in Example 4.3.

As concerns $k_{eff}(\theta)$, we have the exact match $k_{eff}(\theta) = k^H(\theta)$ which depends only on the current volume fraction $\widetilde{\chi_{eff}}(\theta)$ rather than the actual possible arrangements of $\omega_l^{(w)}$ corresponding to this θ. In the example, we can compare the use of the weighted averages k^A, k^G calculated from the same data.

Example 5.3 (comparison of solutions to Model-ω-extended applied at every cell of Model-Ω-extended). The solutions $(\theta^\epsilon, w^\epsilon)$ and $(\widetilde{\theta^{eff}}, \widetilde{w^{eff}})$ are approximated independently of one another with spatial discretization corresponding to $M^\epsilon = 1000$ and $M^{eff} = 25$ cells, respectively. We also use finer time-stepping for the pore-scale $\tau^\epsilon = 1$[s] than that for the Darcy scale model where $\tau^{eff} = 10$[s]. The solutions (θ, w) at the end $T = 10,000$ are plotted in Figure 13. We also plot the normal fluxes at $x = 0$ (left boundary) and $x = 10$ (right boundary) in Figure 14.

We now compare the pore-scale solutions to Model-ω-extended with the REV ω distributed over all Ω to the solutions to Model-Ω-extended-fit approximating the effective Model-Ω-extended. We observe that the pointwise values of θ^ϵ are close to $\widetilde{\theta^{eff}}$. In addition, the values of $\widetilde{w^{eff}}$ are quite visibly in the "middle" between the lower and upper bounds of w^ϵ which correspond to the rock and water portions of each $\omega^{(r)}$, and $\omega^{(w)}$, respectively. One interesting feature is the presence of the individual pointwise "spikes" in w^ϵ which correspond to the temperatures θ^ϵ crossing the different freezing temperatures specific to the different material types in every REV ω. We also see the expected "wiggles" of θ^ϵ around θ^{eff}. Finally, the closeness of θ^ϵ and $\widetilde{\theta^{eff}}$ is most pronounced for the "correct" and exact $k^H = k_{eff}$.

Further insight is provided through the analysis of fluxes in Figure 14. We see that the right flux quickly settles to an inflow energy value already around $t = 1000$, with the closest agreement from the simulation corresponding to k^H. The left flux is of much smaller magnitude of about 10% of the right. The time oscillations in flux visible from pore scale correspond to the finite time of propagation of free boundary across the cells, and are typical for the solutions to Stefan problem, and more general, for any phase change problems.

5.4.1. Performance of our computational algorithm. We also briefly report on the performance of our P0-P0 algorithm when applied to Example 5.3. We have performed an extensive study of our P0-P0 algorithm at the pore scale in [6]; therefore, we only report about the algorithm at the Darcy scale. Convergence was

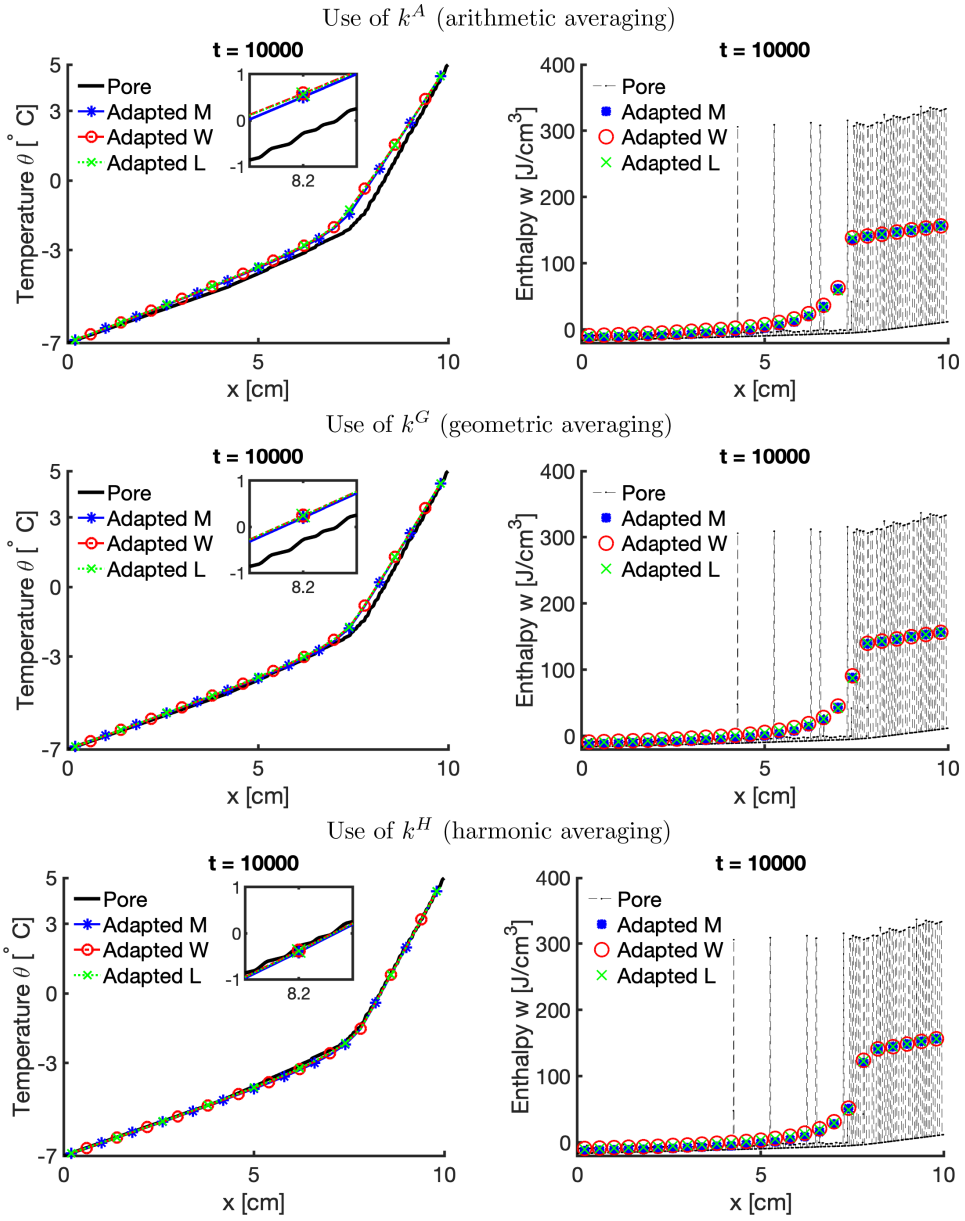

FIG. 13. *Illustration for Example* 5.3*: plots of temperature* θ *(left) and enthalpy (right)* w *at* $t = 10,000$ [s] *of solutions to Model-*ω*-extended and Model-*Ω*-extended at the pore and Darcy scale, respectively. Very good agreement of the pore-scale with the Darcy-scale solutions is visible; it is excellent when* k^H *is used.*

achieved for grid sizes $h \in \{0.4, 0.2, 0.1\} \times 10^{-2}$ [m] and $\tau \in \{1, 10, 100\}$ [s]. The L, W, and M models have similar performance with a maximum of 4–9 iterations and mean of 2–4.2 iterations. For time steps $\tau = 1, 10$ and 100, time step reduction was observed until $\tau = 0.5, 2.5$, and 50, respectively, and the number of iterations decrease with decreasing time step. Moreover, no difference was observed when using $k^P = k^A, k^G$ or k^H. More analysis will be given in [74].

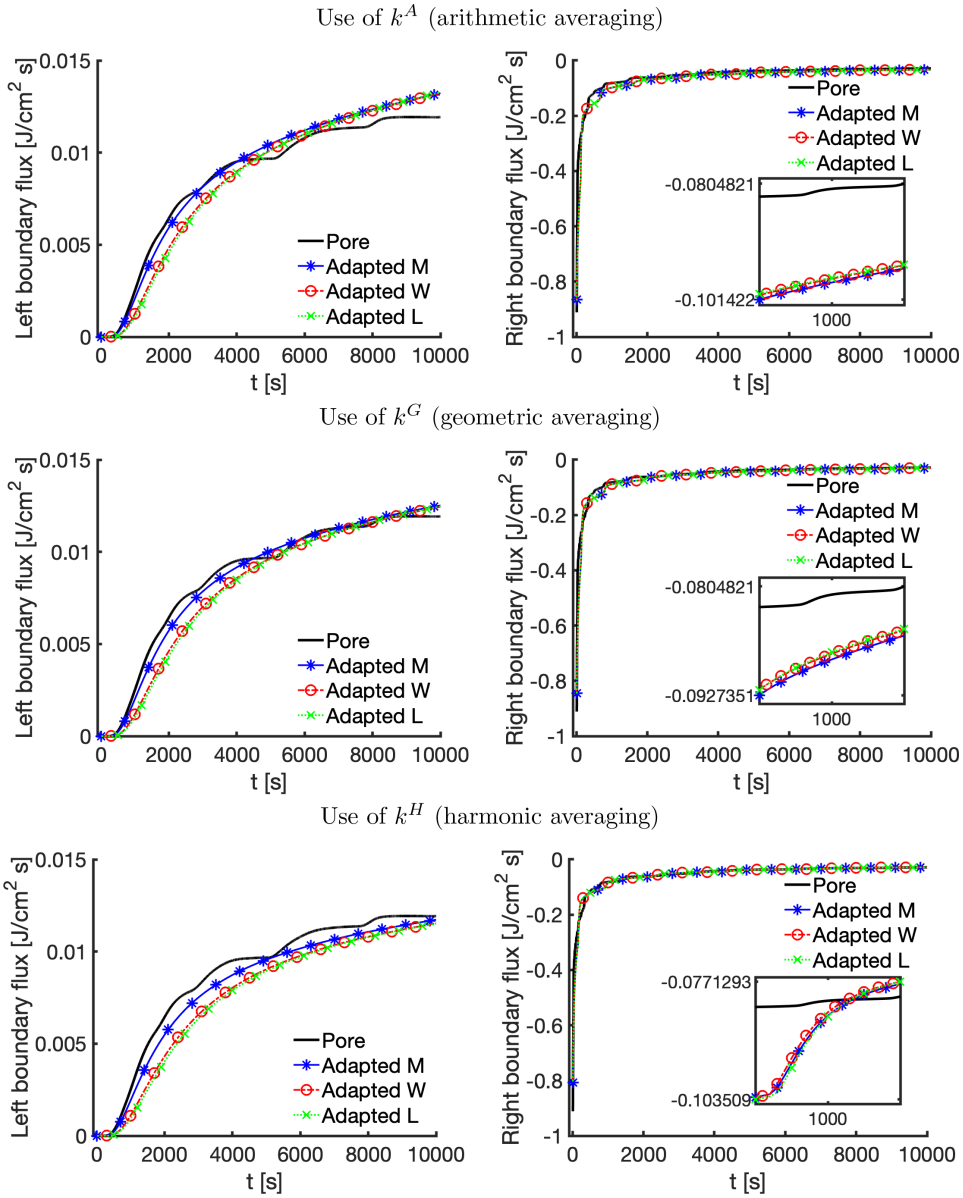

FIG. 14. *Illustration of Example* 5.3*: plot of the left and right boundary heat fluxes* $q(t)$ *in time. The inset is chosen at* $t = 1000$ *when the phase change is first well visible.*

6. Summary and conclusions. In this paper we consider upscaling of heterogeneous Stefan problem which features multiple nonlinearities, some of which are multivalued; all are dependent on the type of material considered.

We apply rigorous theory from [73] and derive practical formulas for the effective properties in section 3. First, we consider the Model-ω-basic for the rock and water mixture at the pore-scale which we upscale to the Darcy-scale Model-Ω-basic. We demonstrate that additional microscale physics must be incorporated and thus we

propose Model-ω-extended, which after upscaling to Model-Ω-extended shows qualitative agreement with Model-Ω-empirical. We also propose a reduced model for handling effective conductivities. In the end, the solutions of upscaled and micromodel compare well.

The theoretical contributions of this work include a new connection between the pore- and the Darcy-scale models, a method to incorporate microphysics in the rigorous upscaling process, and a new proposed reduced model for effective conductivities which honors the underlying uncertainty.

The practical contribution is that we are able to relate the pore-scale properties of porous media such as pore distribution to the effective properties such as water content $\chi_l^P(\theta)$. This practical relationship allows one to construct the effective constitutive properties of permafrost "in silicio" instead of via experiments. One other important take-away message is that some of the approximations commonly used in the Darcy-scale models including the arithmetic or geometric weighting of conductivities might lead to modeling errors.

More research is underway addressing some of the open questions. In particular, in this paper we only considered the continuous relationships $\chi_l^P(\theta)$ which we adapted from the models in literature, and only simulated upscaled models with their effective approximations $\widetilde{\chi_{eff}^{model}}$. More general study as well as development of algorithms for properties involving the mixtures of step functions is needed. Moreover, we only studied a portion of the microphysics by including freezing point depression. More can be incorporated in future models.

Furthermore, we only considered air-free media, and only studied thermal models. More general coupled thermal–hydrological models will be considered in the future.

A. Appendix. We include here additional notes on theoretical background and computational results.

A.1. Additifonal theoretical notes. We now provide now detailed theoretical results in abstract spaces related to the material in section 3.1.1 which set the stage for Proposition 3.1.

Remark 7.1. With the hypotheses in section 3.1.1, [73, Thm. 3.1] establishes the existence of a solution $w \in L^\infty(L^2)$, and [73, Thm, 4.1] proves two-scale convergence as $\epsilon \to 0$. The coarse-scale problem in [73, Prob. 5.1 and Thm. 5.4] requires additional assumptions [73, eqs. (5.1)–(5.3)] on the dependence of q on u [these hold for $q = -k(\theta, x, y)\nabla\theta(x, y)$ considered in this paper]. The effective conductivity K_0 [our k_{eff}] calculations are in [73, eqs. (6.1)–(6.7)]. The simplified cases listed in [73, eqs. (6.8)–(6.9)] do not apply to the composite materials in this paper. Furthermore, [73, Thms. 4.1 and 5.1] prove two-scale convergence of the solutions of the ϵ problem [73, Prob 3.1] and derive the two scale equation [73, eqs. (5.8)–(5.11) or Prob. 5.1] satisfied by the asymptotic limits, as well as the coarse scale problem with data $\partial\psi_0, K_0$ [our α_{eff}, k_{eff}] defined by [73, Thm. 5.4], [73, eqs. (6.6)–(6.7)], respectively.

7.2. Data on parameters and fitting. We include here the tables with parameters and reporting on the data fitting. Table 7 provides summary of the adapted χ_l^P models.

Table 8 contains details on these parametric models in Example 4.2.

Table 9 presents results of fitting of χ_{eff} to these parametric models in Examples 4.3 and 4.5.

TABLE 7
Parameters for soil freezing curves SFC for clay. These are used for the plots of SFC in Figure 2.

Model	$\chi_I^P(\theta)\|_{\theta<\theta_*}$	Parameters	Reference
L [34]	$a\|\theta\|^b$	$a=1.0397$ [−], $b=-0.271$ [−], $\theta_*=0$ [°C]	[34, Figure 9]
W [75]	$a\left(\frac{b}{b-\theta+\theta_*}\right)^4+\chi_{res}$	$a=0.4$ [−], $b=7.22$ [°C], $\chi_{res}=0.36$ [−], $\theta_*=0$ [°C]	[75, Table 3]
M [38]	$(a-\chi_{res})e^{b(\theta-\theta_*)}+\chi_{res}$	$a=0.989$ [−], $b=0.16$ [1/°C], $\chi_{res}=0.201$ [−], $\theta_*=0$ [°C]	[78, p. 7]
Adapted L	$\|\theta_*\|^b\|\theta\|^{-b}$	$b=0.271$ [−], $\theta_*=-1.1544$ [°C]	
Adapted W	$(1-\chi_{res})\left(\frac{b}{b-\theta+\theta_*}\right)^4+\chi_{res}$	$b=6.4216$ [°C], $\chi_{res}=0.36$ [−], $\theta_*=0$ [°C]	
Adapted M	$\chi_{res}+(1-\chi_{res})e^{b(\theta-\theta_*)}$	$b=0.16$ [1/°C], $\chi_{res}=0.20144$ [−] $\theta_*=0$ [°C]	

TABLE 8

Parameters for model $= L, W, M$ in Example 4.2 found by fitting χ_{eff} shown in Figure 5 to $\widetilde{\chi_{eff}^{model}}$. Rightmost column shows literature values and ranges.

Model/Unit	Parameter $\chi_{res}[-]$					
		$N_{WMAT} = 10$		$F = 10^{-3}$		
	$F = 5 \times 10^{-4}$	$F = 10^{-3}$	$F = 2 \times 10^{-3}$	$N_{WMAT} = 5$	$N_{WMAT} = 20$	Literature
Adapted L	NA	NA	NA	NA	NA	-
Adapted W [–]	1.307×10^{-2}	2.506×10^{-2}	3.937×10^{-2}	1.228×10^{-2}	4.710×10^{-2}	$\{0.12, 0.36\}$ [75, Tab. III]
Adapted M [–]	1.802×10^{-2}	3.575×10^{-2}	6.476×10^{-2}	1.748×10^{-2}	7.124×10^{-2}	$\{0.081, 0.2014\}$ [38,p. 56], [78, p. 7]
	Parameter b					
		$N_{WMAT} = 10$		$F = 10^{-3}$		
	$F = 5 \times 10^{-4}$	$F = 10^{-3}$	$F = 2 \times 10^{-3}$	$N_{WMAT} = 5$	$N_{WMAT} = 20$	Literature
Adapted L [–]	1.570	1.557	1.553	1.496	1.560	$\{0.197, 0.271, 0.393\}$ [34, Fig. 9], $[0.097, 1.13]$ [1, p. 32, Tabs. 2–6]
Adapted W [°C]	1.502	2.808	5.218	1.708	4.877	$\{1.11,\ 7.22\}$ [75, Tab. III]
Adapted M [1/°C]	2.001	1.101	6.443×10^{-1}	1.702	6.920×10^{-1}	$\{0.9, 0.16\}$ [38, p. 56], [78, p. 7]
	Freezing point depression θ_*					
		$N_{WMAT} = 10$		$F = 10^{-3}$		
	$F = 5 \times 10^{-4}$	$F = 10^{-3}$	$F = 2 \times 10^{-3}$	$N_{WMAT} = 5$	$N_{WMAT} = 20$	Literature
Adapted L [°C]	-3.954×10^{-1}	-7.873×10^{-1}	-1.573	-3.845×10^{-1}	-1.571	-
Adapted W [°C]	-3.460×10^{-1}	-7.086×10^{-1}	-1.456	-2.915×10^{-1}	-1.498	0 [75, (p. 16]
Adapted M [°C]	-2.916×10^{-1}	-6.190×10^{-1}	-1.352	-2.032×10^{-1}	-1.415	0 [38, p. 56], [78, p. 7]

TABLE 9
The parameters of fitted models model = L, W, M for fitting χ_{eff} to $\widetilde{\chi_{eff}^{model}}$.

Example 4.3(a)		$b^L = 2.6973, \theta_*^L = -0.80199,$ $b^W = 1.3709, \theta_*^W = -0.80007, \chi_{res}^W = 0,$ $b^M = 2.4568, \theta_*^M = -0.80247, \chi_{res}^M = 0.$
Example 4.3(b)		$b^L = 2.6075, \theta_*^L = -1.4665$ $b^W = 2.6393, \theta_*^W = -1.4526, \chi_{res}^W = 0$ $b^M = 1.2245, \theta_*^M = -1.4348, \chi_{res}^M = 0$
Example 4.5(a)	[59]	$b^L = 7.816 \times 10^{-1}, \theta_*^L = -8.871 \times 10^{-4},$ $b^W = 7.428 \times 10^{-3}, \theta_*^W = -8.623 \times 10^{-4}, \chi_{res}^W = 0,$ $b^M = 4.821 \times 10^{2}, \theta_*^M = -8.519 \times 10^{-4}, \chi_{res}^M = 0.$
Example 4.5(b)	[29]	$b^L = 8.586 \times 10^{-1}, \theta_*^L = -2.659 \times 10^{-3},$ $b^W = 1.872 \times 10^{-2}, \theta_*^W = -2.670 \times 10^{-3}, \chi_{res}^W = 0,$ $b^M = 1.940 \times 10^{2}, \theta_*^M = -2.668 \times 10^{-3}, \chi_{res}^M = 0.$

Acknowledgments. The authors wish to thank the anonymous reviewers for their remarks, which helped to improve the exposition in this paper.

REFERENCES

[1] O. B. Andersland and B. Ladanyi, *Frozen Ground Engineering*, 2nd ed., Wiley, ASCE, Hoboken, NJ, Reston, VA, 2004.

[2] D. M. Anderson and A. R. Tice, *Predicting Unfrozen Water Contents in Frozen Soils from Surface Area Measurements*, Highway Research Record, 1972.

[3] T. Arbogast, M. F. Wheeler, and N.-Y. Zhang, *A nonlinear mixed finite element method for a degenerate parabolic equation arising in flow in porous media*, SIAM J. Numer. Anal., 33 (1996), pp. 1669–1687, https://doi.org/10.1137/S0036142994266728.

[4] J. Bear and A. Cheng, *Modeling Groundwater Flow and Contaminant Transport*, Vol. 23, Springer, Dordrecht, 2010, https://doi.org/10.1007/978-1-4020-6682-5.

[5] L. Bigler, *Computational Modeling of Phase Change at Different Scales with Applications*, Ph.D. thesis, Oregon State University, Corvallis, Oregon, 2022.

[6] L. Bigler, M. Peszynska, and N. Vohra, *Heterogeneous Stefan problem and permafrost models with P0-P0 finite elements and fully implicit monolithic solver*, Electron. Res. Arch., 30 (2022), pp. 1477–1531, https://doi.org/10.3934/era.2022078.

[7] C. Bringedal, I. Berre, I. Pop, and F. Radu, *Upscaling of non-isothermal reactive porous media flow with changing porosity*, Transp. Porous Media, 114 (2016), pp. 371–393.

[8] M. K. Brun, I. Berre, J. M. Nordbotten, and F. A. Radu, *Upscaling of the coupling of hydromechanical and thermal processes in a quasi-static poroelastic medium*, Transp. Porous Media, 124 (2018), pp. 137–158.

[9] C. Calvo-Jurado and W. J. Parnell, *Hashin–Shtrikman bounds on the effective thermal conductivity of a transversely isotropic two-phase composite material*, J. Math. Chem., 53 (2015), pp. 828–843.

[10] J. Chu, B. Engquist, M. Prodanović, and R. Tsai, *A multiscale method coupling network and continuum models in porous media* I*: Steady-state single phase flow*, Multiscale Model. Simul., 10 (2012), pp. 515–549, https://doi.org/10.1137/110836201.

[11] D. D. Cortes, A. I. Martin, T. S. Yun, F. M. Francisca, J. C. Santamarina, and C. Ruppel, *Thermal conductivity of hydrate-bearing sediments*, J. Geophys. Res., 114 (2009).

[12] T. B. Costa, K. Kennedy, and M. Peszynska, *Hybrid three-scale model for evolving pore-scale geometries*, Comput. Geosci., 22 (2018), pp. 925–950, https://doi.org/10.1007/s10596-018-9733-9.

[13] A. Damlamian, *How to homogenize a nonlinear diffusion equation: Stefan's problem*, SIAM J. Math. Anal., 12 (1981), pp. 306–313, https://doi.org/10.1137/0512028.

[14] T. De Kock, M. A. Boone, T. De Schryver, J. Van Stappen, H. Derluyn, B. Masschaele, G. De Schutter, and V. Cnudde, *A pore-scale study of fracture dynamics in rock using X-ray micro-CT under ambient freeze–thaw cycling*, Environ. Sci. Technol., 49 (2015), pp. 2867–2874.

[15] L. J. Durlofsky, *Numerical calculation of equivalent grid block permeability tensors for heterogeneous porous media*, Water Resour. Res., 27 (1991), pp. 699–708, https://doi.org/10.1029/91WR00107.
[16] Y. Efendiev, *Multiscale Finite Element Methods: Theory and Applications*, Surv. Tutor. Appl. Math. Sci. 4, Springer, New York, 2009.
[17] F. Gibou, R. P. Fedkiw, L.-T. Cheng, and M. Kang, *A second-order-accurate symmetric discretization of the Poisson equation on irregular domains*, J. Comput. Phys., 176 (2002), pp. 205–227.
[18] S. Gupta, *The Classical Stefan Problem: Basic Concepts, Modelling and Analysis*, Elsevier Science, 2003.
[19] S. Gärttner, P. Frolkovič, P. Knabner, and N. Ray, *Efficiency and accuracy of micro-macro models for mineral dissolution*, Water Resour. Res., 56 (2020).
[20] R. L. Harlan, *Analysis of coupled heat-fluid transport in partially frozen soil*, Water Resour. Res., 9 (1973), pp. 1314–1323.
[21] D. Hillel, *Fundamentals of Soil Physics*, Academic Press, 1980, https://doi.org/10.1016/C2009-0-03109-2.
[22] U. Hornung, *Homogenization and Porous Media*, Interdiscip. Appl. Math. 6, Springer-Verlag, New York, 1997.
[23] E. E. Jafarov, S. S. Marchenko, and V. E. Romanovsky, *Numerical modeling of permafrost dynamics in Alaska using a high spatial resolution dataset*, Cryosphere, 6 (2012), pp. 613–624, https://doi.org/10.5194/tc-6-613-2012.
[24] A. Jan, E. T. Coon, and S. L. Painter, *Evaluating integrated surface/subsurface permafrost thermal hydrology models in ats (v0.88) against observations from a polygonal tundra site*, Geosci. Model Dev., 13 (2020), pp. 2259–2276.
[25] X. Jiang and R. Nochetto, *A P^1–P^1 finite element method for a phase relaxation model I: Quasiuniform mesh*, SIAM J. Numer. Anal., 35 (1998), https://doi.org/10.1137/S0036142996297783.
[26] T. Kelley and J. Rulla, *Solution of the discretized Stefan problem by Newton's method*, Nonlinear Anal., 14 (1990), pp. 851–872.
[27] T. Kozlowski, *A semi-empirical model for phase composition of water in clay-water systems*, Cold Reg. Sci. Technol., 49 (2007), pp. 226–236.
[28] B. L. Kurylyk and K. Watanabe, *The mathematical representation of freezing and thawing processes in variably-saturated, non-deformable soils*, Adv. Water Resour., 60 (2013), pp. 160–177, https://doi.org/10.1016/j.advwatres.2013.07.016.
[29] L. W. Lake, *Enhanced Oil Recovery*, Prentice Hall, Englewood Cliffs, NJ, 1989.
[30] F. Ling and T. Zhang, *A numerical model for surface energy balance and thermal regime of the active layer and permafrost containing unfrozen water*, Cold Reg. Sci. Technol., 38 (2004), pp. 1–15, https://doi.org/10.1016/S0165-232X(03)00057-0.
[31] R. Lipton and B. Vernescu, *Composites with imperfect interface*, Proc. Roy. Soc. Lond. Ser. A Math. Phys. Sci., 452 (1996), pp. 329–358.
[32] T. Little and R. Showalter, *The super-Stefan problem*, Internat. J. Engrg. Sci., 33 (1995), pp. 67–75.
[33] H. Liu, P. Maghoul, A. Shalaby, and A. Bahari, *Thermo-hydro-mechanical modeling of frost heave using the theory of poroelasticity for frost-susceptible soils in double-barrel culvert sites*, Transp. Geotech., 20 (2019), 100251, https://doi.org/10.1016/j.trgeo.2019.100251.
[34] C. W. Lovell, *Temperature effects on phase composition and strength of partially-frozen soil*, Highway Res. Board Bull., (1957), pp. 74–95, https://trid.trb.org/view/128123.
[35] E. Magenes, R. H. Nochetto, and C. Verdi, *Energy error estimates for a linear scheme to approximate nonlinear parabolic problems*, ESAIM: M2AN, 21 (1987), pp. 655–678, https://doi.org/10.1051/m2an/1987210406551.
[36] C. C. Mei and B. Vernescu, *Homogenization Methods for Multiscale Mechanics*, World Scientific, Singapore, 2010, https://cds.cern.ch/record/1413771.
[37] G. H. Meyer, *Multidimensional Stefan problems*, SIAM J. Numer. Anal., 10 (1973), pp. 522–538, https://doi.org/10.1137/0710047.
[38] R. L. Michalowski, *A constitutive model of saturated soils for frost heave simulations*, Cold Reg. Sci. Technol., 22 (1993), pp. 47–63, https://doi.org/10.1016/0165-232X(93)90045-A.
[39] D. Nicolsky, V. Romanovsky, and G. Panteleev, *Estimation of soil thermal properties using in-situ temperature measurements in the active layer and permafrost*, Cold Reg. Sci. Technol., 55 (2009), pp. 120–129, https://doi.org/10.1016/j.coldregions.2008.03.003.

[40] D. Nicolsky, V. Romanovsky, and G. Tipenko, *Using in-situ temperature measurements to estimate saturated soil thermal properties by solving a sequence of optimization problems*, Cryosphere, 1 (2007), pp. 41–58, https://doi.org/10.5194/tc-1-41-2007.

[41] R. H. Nochetto and C. Verdi, *The combined use of a nonlinear Chernoff formula with a regularization procedure for two-phase Stefan problems*, Numer. Funct. Anal. Optim., 9 (1988), pp. 1177–1192, https://doi.org/10.1080/01630568808816279.

[42] T. E. Osterkamp, *Freezing and thawing of soils and permafrost containing unfrozen water or brine*, Water Resour. Res., 23 (1987), pp. 2279–2285.

[43] G. Papanicolau, A. Bensoussan, and J. L. Lions, *Asymptotic Analysis for Periodic Structures*, North Holland, 1978.

[44] M. Peszynska and R. Showalter, *Approximation of scalar conservation law with hysteresis*, SIAM J. Numer. Anal., 58 (2020), pp. 962–987, https://doi.org/10.1137/18M1197679.

[45] M. Peszynska, R. Showalter, and S.-Y. Yi, *Flow and transport when scales are not separated: Numerical analysis and simulations of micro- and macro-models*, Int. J. Numer. Anal. Model., 12 (2015), pp. 476–515, http://www.math.ualberta.ca/ijnam/Volume-12-2015/No-3-15/2015-03-04.pdf.

[46] M. Peszynska and R. E. Showalter, *Approximation of hysteresis functional*, J. Comput. Appl. Math., 389 (2021), 113356.

[47] M. Peszynska and A. Trykozko, *Convergence and stability in upscaling of flow with inertia from porescale to mesoscale*, Int. J. Multiscale Comput. Eng., 9 (2011), pp. 215–229, https://doi.org/10.1615/IntJMultCompEng.v9.i2.60.

[48] M. Peszynska and A. Trykozko, *Pore-to-core simulations of flow with large velocities using continuum models and imaging data*, Comput. Geosci., 17 (2013), pp. 623–645, https://doi.org/10.1007/s10596-013-9344-4.

[49] M. Peszynska, A. Trykozko, G. Iltis, S. Schlueter, and D. Wildenschild, *Biofilm growth in porous media: Experiments, computational modeling at the porescale, and upscaling*, Adv. Water Resour., 95 (2016), pp. 288–301.

[50] M. Peszynska, J. Umhoefer, and C. Shin, *Reduced model for properties of multiscale porous media with changing geometry*, Computation, 9 (2021), 28, https://doi.org/10.3390/computation9030028.

[51] I. Pop, F. Radu, and P. Knabner, *Mixed finite elements for the Richards' equation: Linearization procedure*, J. Comput. Appl. Math., 168 (2004), pp. 365–373, https://doi.org/10.1016/j.cam.2003.04.008.

[52] A. Quarteroni, *Reduced Basis Methods for Partial Differential Equations: An Introduction*, Springer, Cham, 2016.

[53] F. Radu, I. Pop, and P. Knabner, *Error estimates for a mixed finite element discretization of some degenerate parabolic equations*, Numer. Math., 109 (2008), pp. 285–311, https://doi.org/10.1007/s00211-008-0139-9.

[54] F. Radu, I. S. Pop, and P. Knabner, *Order of convergence estimates for an Euler implicit, mixed finite element discretization of Richards' equation*, SIAM J. Numer. Anal., 42 (2004), pp. 1452–1478, https://doi.org/10.1137/S0036142902405229.

[55] N. Ray, A. Rupp, R. Schulz, and P. Knabner, *Old and new approaches predicting the diffusion in porous media*, Transp. Porous Media, 124 (2018), pp. 803–824.

[56] A. W. Rempel and L. J. V. Alst, *Potential gradients produced by pore-space heterogeneities: Application to isothermal frost damage and submarine hydrate anomalies*, in Proceedings of the Fifth Biot Conference on Poromechanics, 2013, pp. 813–822, https://doi.org/10.1061/9780784412992.098.

[57] J. Ren, S. Vanapalli, and Z. Han, *Soil freezing process and different expressions for the soil-freezing characteristic curve*, Sci. Cold Arid Regions, 9 (2017), pp. 221–228, http://www.scar.ac.cn/EN/10.3724/SP.J.1226.2017.00221.

[58] J. C. Rogers, A. E. Berger, and M. Ciment, *The alternating phase truncation method for numerical solution of a Stefan problem*, SIAM J. Numer. Anal., 16 (1979), pp. 563–587, https://doi.org/10.1137/0716043.

[59] E. C. Rooney, V. L. Bailey, K. F. Patel, M. Dragila, A. K. Battu, A. C. Buchko, A. C. Gallo, J. Hatten, A. R. Possinger, O. Qafoku, L. Reno, M. SanClements, T. Varga, and R. A. Lybrand, *Soil pore network response to freeze-thaw cycles in permafrost aggregates*, Geoderma, 411 (2022), 115674, https://doi.org/10.1016/j.geoderma.2021.115674.

[60] T. Roubicek, *The Stefan problem in heterogeneous media*, Ann. Inst. H. Poincaré Anal. Non Linéaire, 6 (1989), pp. 481–501.

[61] J. Rulla and N. J. Walkington, *Optimal rates of convergence for degenerate parabolic problems in two dimensions*, SIAM J. Numer. Anal., 33 (1996), pp. 56–67, https://doi.org/10.1137/0733004.

[62] E. E. Sanchez-Palencia, *Non-homogenous Media and Vibration Theory*, Lecture Notes in Physics, Springer-Verlag, Berlin, 1980.
[63] E. Schneid, P. Knabner, and F. Radu, *A priori error estimates for a mixed finite element discretization of the Richards' equation*, Numer. Math., 98 (2004), pp. 353–370.
[64] C. Shin, A. Alhammali, L. Bigler, N. Vohra, and M. Peszynska, *Coupled flow and biomass-nutrient growth at pore-scale with permeable biofilm, adaptive singularity and multiple species*, Math. Biosci. Eng., 18 (2021), pp. 2097–2149, https://doi.org/10.3934/mbe.2021108.
[65] R. E. Showalter, *Mathematical formulation of the Stefan problem*, Internat. J. Engrg. Sci., 20 (1982), pp. 909–912, https://doi.org/10.1016/0020-7225(82)90109-4.
[66] R. E. Showalter, *Monotone Operators in Banach Space and Nonlinear Partial Differential Equations*, Math. Surveys Monogr. 49, American Mathematical Society, Providence, RI, 1997, https://doi.org/10.1090/surv/049.
[67] J. C. Stuurop, S. E. A. T. M. van der Zee, C. I. Voss, and H. K. French, *Simulating water and heat transport with freezing and cryosuction in unsaturated soil: Comparing an empirical, semi-empirical and physically-based approach*, Adv. Water Resour., 149 (2021), 103846, https://doi.org/10.1016/j.advwatres.2021.103846.
[68] V. R. Tarnawski and B. Wagner, *Modeling the thermal conductivity of frozen soils*, Cold Reg. Sci. Technol., 22 (1993), pp. 19–31.
[69] L. Tartar, *Incompressible Fluid Flow in a Porous Medium Convergence of the Homogenization Process*, Appendix Lect. Notes Phys. 127, Springer-Verlag, Berlin, 1980.
[70] A. Trykozko, M. Peszynska, and M. Dohnalik, *Modeling non-Darcy flows in realistic porescale proppant geometries*, Comput. Geotech., 71 (2015), pp. 352–360, https://doi.org/10.1016/j.compgeo.2015.08.011.
[71] C. Verdi and A. Visintin, *Error estimates for a semi-explicit numerical scheme for Stefan-type problems*, Numer. Math., 52 (1987/88), pp. 165–186, http://eudml.org/doc/133231.
[72] A. Visintin, *Models of Phase Transitions*, Progr. Nonlinear Differential Equations Appl. 28, Birkhäuser Boston, Boston, MA, 1996, https://doi.org/10.1007/978-1-4612-4078-5.
[73] A. Visintin, *Homogenization of a doubly nonlinear Stefan-type problem*, SIAM J. Math. Anal., 39 (2007), pp. 987–1017, https://doi.org/10.1137/060676647.
[74] N. Vohra and M. Peszynska, *Robust conservative scheme and nonlinear solver for phase transitions in heterogeneous permafrost*, J. Comput. Appl. Math., 442 (2024), 115719, https://doi.org/10.1016/j.cam.2023.115719.
[75] J. A. Wheeler, *Simulation of heat transfer from a warm pipeline buried in permafrost*, in AICHE paper 27b Presented at 74th National Meeting of American Institute of Chemical Engineers, 1973, pp. 267–284.
[76] C. S. Woodward and C. N. Dawson, *Analysis of expanded mixed finite element methods for a nonlinear parabolic equation modeling flow into variably saturated porous media*, SIAM J. Numer. Anal., 37 (2000), pp. 701–724, https://doi.org/10.1137/S0036142996311040.
[77] H. Zhang, J. Zhang, Z. Zhang, J. Chen, and Y. You, *A consolidation model for estimating the settlement of warm permafrost*, Comput. Geotech., 76 (2016), pp. 43–50, https://doi.org/10.1016/j.compgeo.2016.02.013.
[78] Y. Zhang and R. Michalowski, *Thermal-hydro-mechanical analysis of frost heave and thaw settlement*, J. Geotech. Geoenvironmental Eng., 141 (2015), 04015027, https://doi.org/10.1061/(ASCE)GT.1943-5606.0001305.